GRENOBLE INP-PHELMA

ORGANISATION EUROPÉENNE POUR LA RECHERCHE NUCLÉAIRE

Hadron collective effects studies for the LHC and FCC-hh project

Final year project

Reactor Physics and Nuclear Engineering Specialty

Academic year 2015-2016

Author:
David AMORIM

Supervisor:
Dr. Nicolò BIANCACCI, CERN BE/ABP/HSC
Nicolo.Biancacci@cern.ch

School supervisor:
Pr. Jean-Marie DE CONTO, UGA-LPSC
deconto@lpsc.in2p3.fr

24 August 2016

Acknowledgements

First and foremost I would like to express my gratitude to my supervisor Nicolò Biancacci. This work is only a glimpse of what I learned during these five months thanks to him. This is only the beginning of a longer journey and I am thankful for his commitment.

I would like also to thank Benoit Salvant, Elias Métral and all the HSC section members for their warm welcome. All the past and present discussions gave me an insight on the vast area of collective effects and I am certain that the future will be as beneficial as today.

I want to express all my gratitude to Jean-Marie de Conto who agreed to be my school supervisor for this work but mostly to have accepted to take part in my forthcoming work.

Contents

Acknowledgements **i**

List of Figures **iii**

List of Tables **v**

1 Elements of accelerator physics **4**
- 1.1 The accelerator model . . . 4
- 1.2 Wakefields induced by the beam and impedances . . . 6

2 Beam instabilities studies with DELPHI **8**
- 2.1 Vlasov's formalism for instability prediction . . . 8
- 2.2 Perturbation formalism . . . 9
- 2.3 Eigenvalues problem . . . 10
- 2.4 Signal created by the perturbation . . . 11

3 Beam stability studies with DELPHI **14**
- 3.1 Basic studies with a resistive wall impedance . . . 14
  - 3.1.1 Resistive wall model . . . 14
  - 3.1.2 Chromaticity scan . . . 16
- 3.2 Effect of the longitudinal distribution . . . 16
  - 3.2.1 Implementation of different longitudinal distributions in DELPHI . . . 17
  - 3.2.2 Comparison of DELPHI's results with analytical predictions . . . 17
- 3.3 TMCI studies . . . 19
  - 3.3.1 Transverse Mode Coupling Instability . . . 19
  - 3.3.2 Purely inductive impedance . . . 20
  - 3.3.3 LHC at injection . . . 23
- 3.4 FCC-hh impedance model and beam stability . . . 23
  - 3.4.1 Accelerator parameters and main components . . . 24
  - 3.4.2 Impedance model for FCC-hh . . . 24
  - 3.4.3 Stability studies with DELPHI . . . 29

Conclusion **33**

Appendix A Derivation of the eigenvalues problem from Sacherer equation **35**
- A.1 Right hand side, damper part . . . 35
- A.2 Left hand side . . . 36

Résumé **39**

Abstract **39**

List of Figures

1 The CERN accelerator complex in 2016 2
2 FCC project situation and accelerator layout, from [4] 3

1.1 The accelerator model: x, y and z are the coordinates of the particle with respect to the synchronous particle 4
1.2 Example of wakefields induced by a beam, from [13] 6
1.3 The tested device of length L, the reference particle is the source of the wakefield acting on the test particle 6
1.4 Beam distribution and induced wakefield on the test particle, from [13] 7

2.1 First Laguerre polynomials for $l = 0$ (left) and for $n = 3$ (right) 11
2.2 Sketch of the longitudinal structure of the beam executing transverse oscillations. Successive snapshots are represented for the first three azimuthal modes. Sketch from A. Chao [7] 12
2.3 Spectrum of some oscillation modes (first row), and the associated signal that could be observed, with a positive chromaticity (second row) and without chromaticity (third row). Sketch from E.Métral [11] 12
2.4 Example of signals obtained with DELPHI for a resistive wall impedance. 13

3.1 Beam pipe model used in the resistive wall impedance simulations. 14
3.2 Horizontal dipolar impedance as a function of frequency for the resistive wall model described in table 3.1. 15
3.3 Most unstable mode tuneshift for a resistive wall impedance, as a function of chromaticity. 16
3.4 The different longitudinal distributions used in DELPHI and their expression in terms of Laguerre polynomials. 18
3.5 Most unstable mode tuneshift for different longitudinal distributions. Scan on bunch intensity for chromaticity $Q' = -3$. Results obtained with DELPHI and linear fitting. 18
3.6 Mode shifts (top) and growth rates (bottom) versus bunch intensity (in protons per bunch) obtained with DELPHI simulations for an FCC-hh impedance model, described in section 3.4.2. Red points indicate the most unstable mode (eigenvalue with the largest imaginary part). 20
3.7 Broadband resonator impedance model used to simulate a constant inductive impedance. 21
3.8 Tune shifts obtained with an inductive impedance. In red DELPHI results with a Gaussian beam. In black Elias Métral eigenvalues obtained for a uniform longitudinal distribution [12]. 22
3.9 Growth rate of the most unstable mode as a function of the chromaticity and bunch intensity for the LHC at injection energy. 23
3.10 Pictures of the LHC and FCC-hh beam screens. 24
3.11 Pictures of a LHC collimator. 26
3.12 Interconnections model for the FCChh, from [8]. 26
3.13 Transverse dipolar impedance in the horizontal plane as a function of frequency for four study cases of FCC-hh. 28
3.14 Transverse dipolar impedance in the vertical plane as a function of frequency for four study cases of FCC-hh. 28

3.15 Beam spectrum $h(\omega)$ as a function of frequency used for the computation of Z_{eff}. . . 28
3.16 Tune shifts and growth rates versus bunch intensity obtained with DELPHI simulations for the cases Beam screen only and Beam screen + graphite collimators. Red points signal the most unstable mode (eigenvalue with the largest imaginary part). 30
3.17 Tune shifts and growth rates versus bunch intensity obtained with DELPHI simulations for the cases Beam screen + Molybdenum-Graphite collimators and Beam screen + Molybdenum-Graphite collimators + interconnects. Red points indicate the most unstable mode (eigenvalue with the largest imaginary part). 31

List of Tables

1 LHC design parameters from [5] and FCC-hh baseline parameters from [6] and [17] . . 2

3.1 Beam parameters and beam pipe model used for the resistive wall study. 15
3.2 Equations of the linear fit performed on mode 0 tuneshift for the different distributions. 19
3.3 Comparison of the ratio of the linear fits slopes versus analytical predictions. 19
3.4 Broadband resonator parameters for the constant inductive impedance model. 21
3.5 FCC-hh main parameters used in the studies. 25
3.6 Resonator parameters for the FCC-hh interconnects model. 27
3.7 Imaginary part of the effective impedance for the four FCChh cases studied. 29
3.8 TMCI threshold estimated with Sacherer formula for the FCChh study cases. 29
3.9 TMCI threshold estimated with Sacherer formula for the FCChh study cases. 30

Introduction

CERN and the accelerator complex

The European Organization for Nuclear Research (CERN) was founded in 1954 with the purpose of bringing together European nations on the common ground of high energy physics research. Nowadays CERN operates three LINACs and seven circular accelerators, whose circumference range from about 30 m for ELENA to almost 27 km for the Large Hadron Collider (LHC). The proton beams energy range goes from a few keV to 6.5 TeV.

The LHC is the most powerful proton collider ever built, presently operating with two beam of 6.5 TeV energy. In order to reach this energy, the beam is pre-accelerated in other machines, as showed in picture 1. The particles extracted from the protons source are accelerated from 100 keV to 50 MeV in the LINAC 2. Then the Proton Synchrotron Booster (PSB), accelerates the beam from 50 MeV to 1.4 GeV. The Proton Synchrotron (PS) then accelerates the beam from 1.4 GeV to 26 GeV. It is important to notice that several important parameters of the LHC's beam such as the transverse quality or the longitudinal structure are set during the acceleration in the PSB and the PS. Finally the Super Proton Synchrotron (SPS) accelerates the beam from 26 GeV to 450 GeV, the LHC injection energy. The LHC gives the last acceleration step itself, the beam energy going from 450 GeV to 6.5 TeV. The LHC can also operate with lead ions, coming from the LINAC 3 and accelerated by the Low Energy Ion Ring (LEIR) before being injected in the PS then the SPS.

Being a collider, one of the LHC significant parameter is the luminosity $\mathcal{L}$. This value is the proportionality factor between the rate of events occuring during a collision $\frac{\mathrm{d}R}{\mathrm{d}t}$ and the cross section of the event σ: $\frac{\mathrm{d}R}{\mathrm{d}t} = \mathcal{L}\sigma$. In the case of two Gaussian beams, the luminosity can be written:

$$L = \frac{n_b N^2 \gamma f_0}{4\pi \sigma_x \sigma_y} \tag{1}$$

with:

- n_b the number of bunches stored in the accelerator;
- N the number of particles per bunches;
- γ the Lorentz factor of the beam;
- f_0 the beam revolution frequency.
- $\sigma_{x,y}$ the transverse RMS beam size;

One can see, to increase the luminosity in order to detect rare events, different ways are possible: increasing the intensity of the beam by increasing the number of bunches and the number of particles per bunches, increasing the beam energy or reducing the beam dimensions at the collision point. But for high intensity beams, the beam itself is a source of electromagnetic fields. The field created by a bunch can perturb the following one or even perturb the same bunch after one complete revolution. In the worst case, these perturbations can make the beam unstable. These collective instabilities have been studied since the late 1950s as the energy of the accelerators increased. As of today accelerator physicists have at their disposal analytic models, numerical and analytical codes to predict beam instabilities in accelerators. These predictions can be compared with measurements performed on past and current machines.

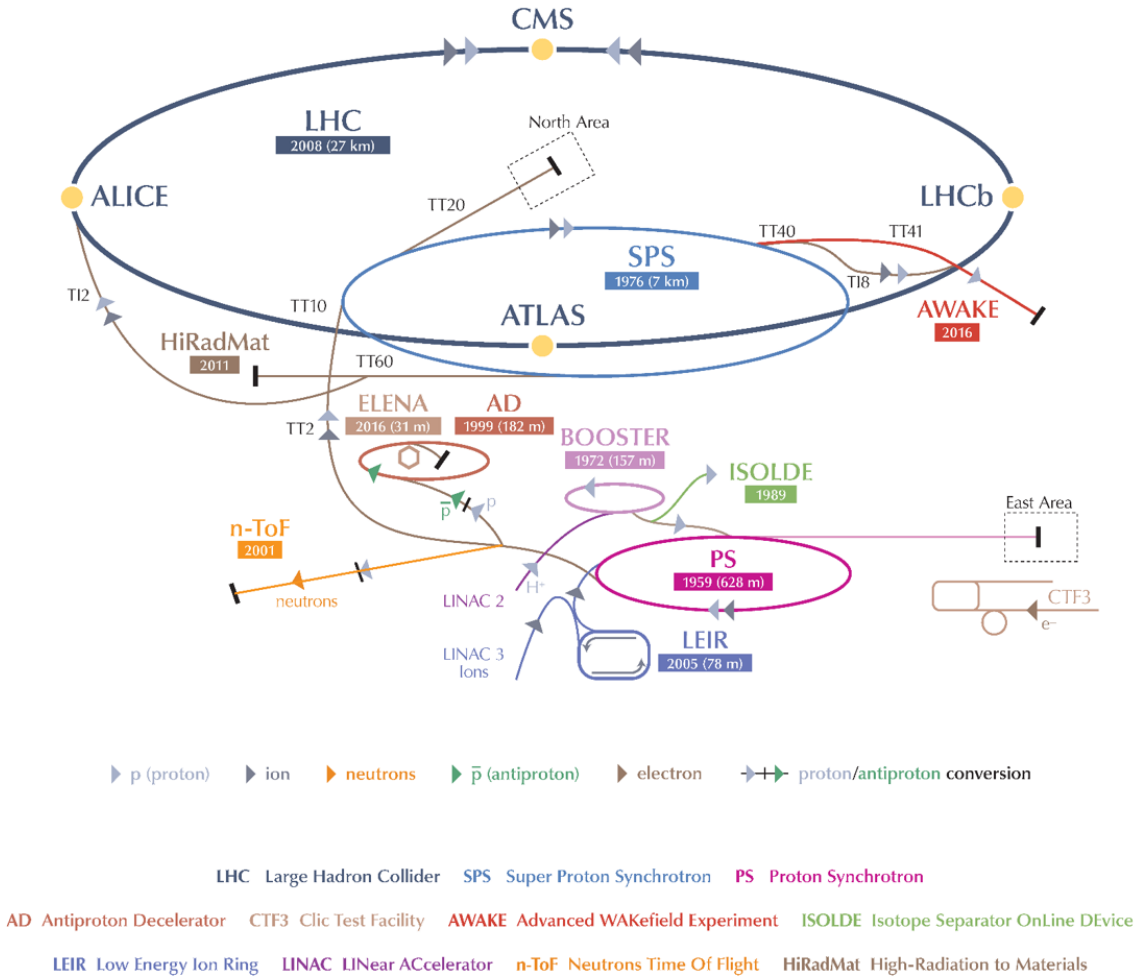

Figure 1: The CERN accelerator complex in 2016

Parameter	LHC	FCC-hh
Beam energy at collision / TeV	7	50
Lorentz factor γ at collision	7461	
Bunch intensity / protons	1.15×10^{11}	1×10^{11}
Number of bunches	2808	10 600
Peak luminosity at interaction point / $\mathrm{cm^{-2} \cdot s^{-1}}$	1×10^{34}	$(5\text{–}20) \times 10^{34}$
Synchrotron radiation / $\mathrm{W \cdot m^{-1}}$	0.17	28.4
Bunch spacing / ns	25	25 or 5
Dipole field / T	8.33	16

Table 1: LHC design parameters from [5] and FCC-hh baseline parameters from [6] and [17]

The FCC project

In order to get most of the capacities of the LHC, the High Luminosty LHC (HL-LHC) upgrade of the LHC aims at increasing the nominal beam current as well as other machine parameters. This upgrade will take place during the LHC long shutdown 2 and 3 in 2019 and 2024 for a start in 2026. However the centre of mass collision energy will remain the same at 14 TeV.

As it is a way to investigate possible new physics, a circular collider with a higher centre of mass collision energy is studied. The FCC-hh is part of the FCC study, which investigate three possible designs: a proton-proton collider (FCC-hh), an electron-positron collider (FCC-ee) and a proton-electron collider (FCC-he). These three projects base themselves on a 100 km long tunnel hosting the accelerator (figure 2). A few parameters for the FCC-hh accelerator are given in table 1.

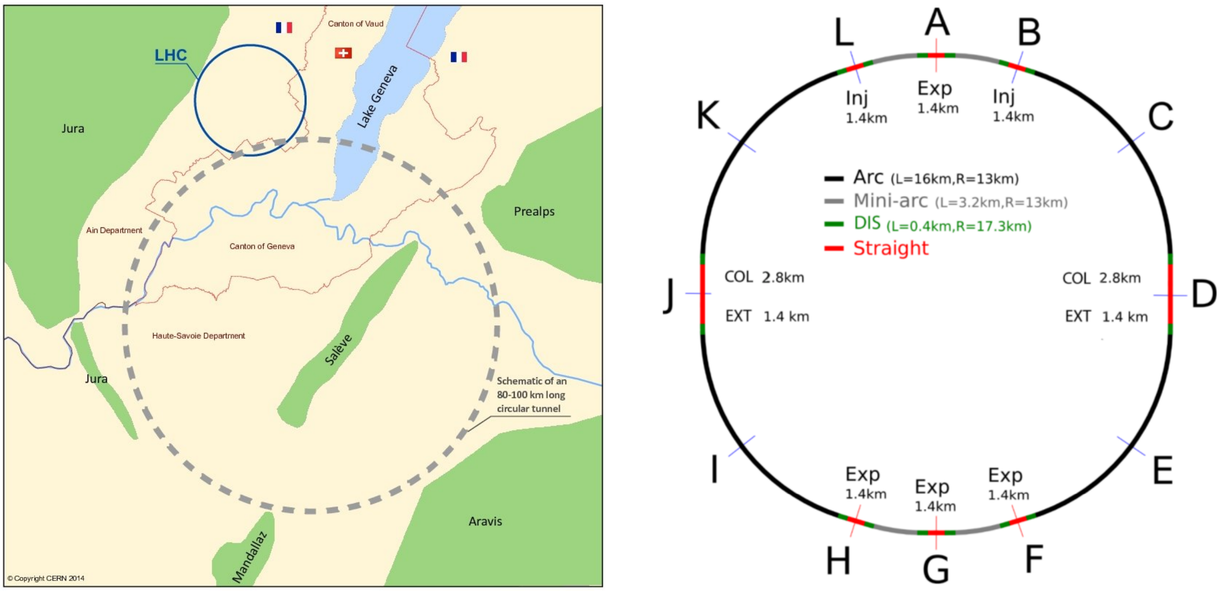

(a) FCC projected situation

(b) FCC-hh projected layout

Figure 2: FCC project situation and accelerator layout, from [4]

Chapter 1

Elements of accelerator physics

This part will first introduce elements of accelerator physics needed to understand the concepts used in beam stability studies. The first part will expose the simple accelerator model used and the second part will explain the concepts of wakefields and impedances which allow to model the effects of self-induced electromagnetic fields on the beam.

1.1 The accelerator model

The circular accelerator will be modelled as a circle of radius R representing the design orbit as in figure 1.1. The synchronous particle is a fictitious particle which follows this design orbit at the design energy. Its position along the accelerator is represented by the coordinate $s = vt$. When the velocity of the synchronous particle is constant, it is possible to use this coordinate as a time variable.

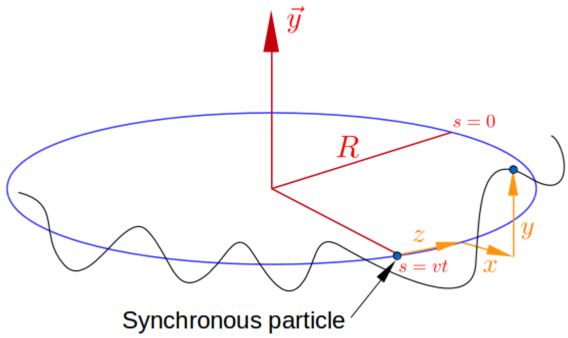

Figure 1.1: The accelerator model: x, y and z are the coordinates of the particle with respect to the synchronous particle

A given particle will be described by a set of six coordinates relative to the the synchronous particle. These six coordinates are $\left(x, x', y, y', z, \frac{\Delta p}{p}\right)$ with $x' = \frac{\mathrm{d}x}{\mathrm{d}s}$ and $y' = \frac{\mathrm{d}y}{\mathrm{d}s}$ the slopes of the horizontal and vertical trajectories and $\frac{\Delta p}{p}$ the relative momentum error of the particle.

The trajectory of an unperturbed, single particle can be described as harmonic oscillators on the x and y planes [7, pp. 8–10],

$$x'' + \frac{\omega_{x0}^2}{R^2\omega_0^2}x = 0 \tag{1.1}$$

$$y'' + \frac{\omega_{y0}^2}{R^2\omega_0^2}y = 0\,, \tag{1.2}$$

where $\omega_0 = \frac{v}{R}$ is the particle angular revolution frequency around the machine, ω_{x_0} and ω_{y_0} are the oscillations frequencies. The betatron tune Q can be introduced as the ratio of the oscillations angular frequency and the revolution angular frequency $Q_{x_0,y_0} = \frac{\omega_{x_0,y_0}}{\omega_0}$. The equations can be rewritten

$$x'' + \frac{Q_{x_0}^2}{R^2} x = 0 \tag{1.3}$$

$$y'' + \frac{Q_{y_0}^2}{R^2} y = 0\,. \tag{1.4}$$

In the longitudinal plane, the particle trajectory can also be described as harmonic oscillators of angular revolution frequency ω_{s_0}. The sychrotron tune is defined as $Q_{s_0} = \frac{\omega_{s_0}}{\omega_0}$. The trajectory equations in the longitudinal plane are

$$z' = -\eta \frac{\Delta p}{p} \tag{1.5}$$

$$\left(\frac{\Delta p}{p}\right)' = \frac{1}{\eta} \frac{Q_{s_0}^2}{R^2} z \tag{1.6}$$

$$z'' + \frac{Q_{s_0}^2}{R^2} z = 0\,, \tag{1.7}$$

where η is the slippage factor. η can be written as $\eta = \frac{1}{\gamma_t^2} - \frac{1}{\gamma^2}$ with $\gamma = \frac{1}{\sqrt{1-\frac{v^2}{c^2}}}$ the Lorentz factor of the particle and γ_t the transition energy. If the particle energy is below the transition energy, $\gamma < \gamma_t$ then $\eta < 0$. Equation 1.5 shows that a particle having a higher momentum than the synchronous particle ($\frac{\Delta p}{p} > 0$) will have its longitudinal coordinate z increasing with time as $z' > 0$. On the other hand, if the particle is above the transition energy then $\eta > 0$. A particle having a higher momentum than the reference particle will slow down as $z' < 0$. This counter-intuitive result is explained by the fact that at high energy the particle velocity is almost equal to the speed of light: a small increase of speed doesn't compensate the increase in the trajectory length, so the particle revolution frequency decrease.

The previous equations suggest that the longitudinal and transverse motions are independent. Actually the motions are linked in multiple ways, one of those link being the chromaticity ξ defined as the variation of the betatron tune with respect to the momentum spread[10, p. 107]

$$\xi = \frac{\Delta Q/Q_0}{\Delta p/p_0}\,. \tag{1.8}$$

The chromatic frequency ω_ξ is defined as

$$\omega_\xi = \frac{\omega_0 Q_0 \xi}{\eta}\,, \tag{1.9}$$

and it can also be represented by

$$Q' = \frac{\eta \omega_\xi}{\omega_0} = Q_0 \xi\,. \tag{1.10}$$

This simple model considers that the beam is unperturbed. If a perturbation is affecting the beam motion in the horizontal plane, equation 1.3 can be written [7, p. 12]

$$x'' + \frac{Q_{x_0}^2}{R^2} x = Kx\,, \tag{1.11}$$

and the perturbed tune can be written $Q_x^2 = Q_{x_0}^2 - KR^2$. If the perturbation is small, the tune shift can be expressed as

$$\Delta Q_x = Q_x - Q_{x_0} = -\frac{KR^2}{2Q_{x_0}}\,. \tag{1.12}$$

In the field of collective effects, computing the tune shifts caused by electromagnetic fields is crucial as it allows to analyse the beam stability. The electromagnetic fields causing these tune shifts can be external (dipole and quadrupole magnets, RF cavities...) or can be produced by the beam itself. These fields can be trapped in some equipment installed along the accelerator, creating resonances and influencing the next beams. The formalism of wakefields and impedances is used to study the effects of these electromagnetic fields on the beam dynamics. This formalism is briefly presented in the next section.

1.2 Wakefields induced by the beam and impedances

Because the environment surrounding the beam is not perfect, the electromagnetic field created by a first bunch can be trapped in the irregularities (see figure 1.2). Depending on their decay rate, these trapped fields can perturb the bunch itself or the following bunches.

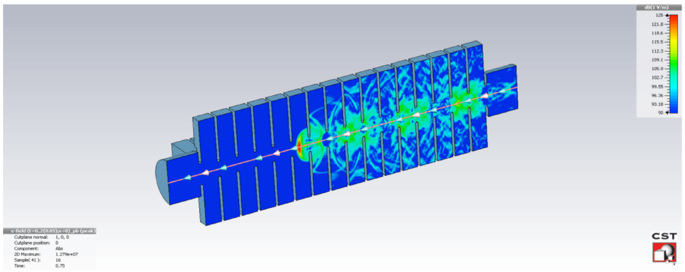

Figure 1.2: Example of wakefields induced by a beam, from [13]

With the wakefields, the goal is to study the force acting on a test particle (in red in figure 1.3) following a reference particle (in blue in figure 1.3) which is the source of the perturbing electromagnetic field. This force can be decomposed in two parts: a longitudinal force which changes the test particle energy and a transverse force which changes its trajectory [13]:

$$\vec{F} = \vec{F}_{\parallel} + \vec{F}_{\perp} \tag{1.13}$$

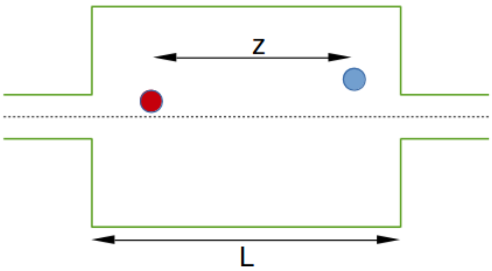

Figure 1.3: The tested device of length L, the reference particle is the source of the wakefield acting on the test particle

When dealing with high energy beams, two approximations can be made:

- the beam is rigid: the perturbation will not affect the motion of the beam as it transits through the structure. It means that the distance z between the two particles remains constant during the transit;
- the charge is not affected by the electromagnetic field but by the impulse given by it: $\Delta\vec{p} = \int \vec{F}\mathrm{d}t$.

In the device of length L pictured in figure 1.3, the integral giving the impulse can be performed over the length L. Using equation 1.13 yields two expressions:

- an energy gain (in J) due to the longitudinal component: $U(z) = \int_0^L F_{\parallel} \mathrm{d}s$, function of the distance z between the reference particle and the test particle;
- a transverse kick (in $\mathrm{N} \cdot \mathrm{m}$) due to the transverse components: $r_0 \vec{M}(z) = \int_0^L \vec{F}_{\perp} \mathrm{d}s$, function of the distance z between the reference particle and the test particle and of the transverse position of the reference particle r_0.

These quantities, when normalized to the charges q^2, are called wakefields:

$$w_{\parallel}(z) = -\frac{U(z)}{q^2} \tag{1.14}$$

$$\vec{w}_{\perp} = \frac{\vec{M}(z)}{q^2} \tag{1.15}$$

When using a distribution such as in figure 1.4, the effect of a slice of the bunch on the test particle is evaluated as:

$$\mathrm{d}U(z) = -e w_{\parallel}(z - z')\lambda(z')\mathrm{d}z' \tag{1.16}$$

the total energy lost or gained by the particle is obtained by summing the contributions of each slice that precedes the test particle:

$$U(z) = -e \int_z^{+\infty} w_{\parallel}\left(z - z'\right) \lambda\left(z'\right) \mathrm{d}z' \tag{1.17}$$

We see that knowing the wakefields allows to compute the energy gain (or loss) or in a similar way the transverse kick given to a particle. These wakefields can also be applied to any distribution of particle. Here they are written in the time domain: for circular machines, because of the periodicity, it can be useful to do a Fourier transform and study the wakefields in the frequency domain. The Fourier transforms of the wakefields are called coupling impedances:

- $Z_{\parallel}(\omega) = \frac{1}{c} \int_{-\infty}^{+\infty} w_{\parallel}(z) \mathrm{e}^{j\frac{\omega z}{c}} \mathrm{d}z$ for the longitudinal impedance (in Ω);
- $\vec{Z}_{\perp}(\omega) = \frac{-j}{c} \int_{-\infty}^{+\infty} \vec{w}_{\perp}(z) \mathrm{e}^{j\frac{\omega z}{c}} \mathrm{d}z$ for the transverse impedance (in $\Omega \cdot \mathrm{m}^{-1}$).

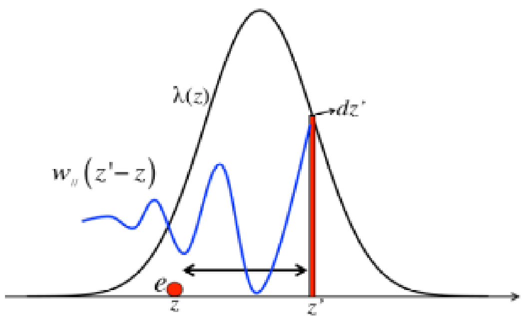

Figure 1.4: Beam distribution and induced wakefield on the test particle, from [13]

In a circular machine, the impedance and wakefields allow to compute the effects of the surrounding environment on the beam. Analytical models exist for simple geometries, allowing to estimate the machine impedance, as presented in [15, chap. 1]. For complex elements of the accelerator numerical models and simulations are often needed because some effects such as resonances can not be predicted analytically.

We now dispose of a theory allowing to represent the effects of the self induced electromagnetic forces acting on the beam. Using the impedance model within Vlasov equation formalism will allow to compute beam stability limits.

Chapter 2

Beam instabilities studies with DELPHI

DELPHI (Discrete Expansion over Laguerre Polynomials and HeadtaIl modes) is a semi-analytical Vlasov solver developed to evaluate the beam transverse stability with respect to the machine's impedance. This part will first expose the Vlasov equation formalism used to get Sacherer integral equation. This equation is then treated to obtain an eigenvalues problem which is solved with DELPHI. Finally the treatment of DELPHI output, a system of eigenvalues and eigenvectors is showed.

2.1 Vlasov's formalism for instability prediction

Vlasov's equation describes the evolution of a particle distribution in phase space. It states that the local phase space distribution density Ψ doesn't change when we follow the particles flow. It can be written

$$\frac{\mathrm{d}\Psi}{\mathrm{d}t} = 0\,. \tag{2.1}$$

The distribution Ψ is a function of the transverse coordinate and momentum y and p_y, as well as the longitudinal coordinate and momentum z and δ. It is also a function of the longitudinal position along the accelerator s, which encloses the time dependence as $s = vt$. Equation 2.1 can be rewritten [7, p. 333]

$$\frac{\partial\Psi}{\partial s} + y'\frac{\partial\Psi}{\partial y} + p_y'\frac{\partial\Psi}{\partial p_y} + z'\frac{\partial\Psi}{\partial z} + \delta'\frac{\partial\Psi}{\partial\delta} = 0\,, \tag{2.2}$$

where the prime is the derivative with respect to s.

The transverse plane coordinates can be changed from position/momentum (y, p_y) to action/angle (J_y, θ_y) [14, pp. 9-10]

$$y = \sqrt{2J_y\frac{R}{Q_{y0}}}\cos(\theta_y) \tag{2.3}$$

$$p_y = \sqrt{2J_y\frac{Q_{y0}}{R}}\sin(\theta_y)\,, \tag{2.4}$$

and Vlasov's equation 2.1 becomes

$$\frac{\partial\Psi}{\partial s} + J_y'\frac{\partial\Psi}{\partial J_y} + \theta_y'\frac{\partial\Psi}{\partial\theta_y} + z'\frac{\partial\Psi}{\partial z} + \delta'\frac{\partial\Psi}{\partial\delta} = 0\,. \tag{2.5}$$

Writing the Hamiltonian H of a single particle will allow, through Hamilton's equations, to express J_y', θ_y', z' and δ' [14, p. 10, p.15][7, pp. 333-334]

$$H = \frac{Q_y}{R} J_y - \frac{1}{2\eta} \left(\frac{\omega_s}{\nu}\right)^2 z^2 - \frac{\eta}{2}\delta^2 - \frac{y}{E} F_y(z,s) \,, \tag{2.6}$$

where $F_y(z,s)$ is the transverse wake force resulting from a dipolar vertical impedance, and E is the particle energy.

With Hamilton's equations, the derivatives with respect to s can be expressed [14, p. 16]

$$J_y' = -\frac{\partial H}{\partial \theta_y} = \frac{\partial y}{\partial \theta_y} \frac{F_y(z,s)}{E} \tag{2.7}$$

$$\theta_y' = \frac{\partial H}{\partial J_y} = \frac{Q_y}{R} - \frac{\partial y}{\partial J_y} \frac{F_y(z,s)}{E} \tag{2.8}$$

$$z' = \frac{\partial H}{\partial \delta} = -\eta\delta \tag{2.9}$$

$$\delta' = -\frac{\partial H}{\partial z} = \left(\frac{\omega_s}{v}\right)^2 \frac{z}{\eta} \,, \tag{2.10}$$

and Vlasov's equation 2.5 now becomes

$$\frac{\partial \Psi}{\partial s} + \frac{F_y(z,s)}{E} \frac{\partial y}{\partial \theta_y} \frac{\partial \Psi}{\partial J_y} + \left(\frac{Q_y}{R} - \frac{F_y(z,s)}{E} \frac{\partial y}{\partial J_y}\right) \frac{\partial \Psi}{\partial \theta_y} - \eta\delta \frac{\partial \Psi}{\partial z} + \left(\frac{\omega_s}{v}\right)^2 \frac{z}{\eta} \frac{\partial \Psi}{\partial \delta} = 0 \,. \tag{2.11}$$

2.2 Perturbation formalism

To treat the stability problem, we assume that a small perturbation ψ_1 of the phase space density develops on top of the unperturbed distribution ψ_0. This mode develops itself with each beam revolution, at a complex frequency $\Omega = Q_c \omega_0$. The total distribution can be written [14, p. 17] [7, p. 334]

$$\psi(s, J_y, \theta_y, z, \delta) = \underbrace{f_0(J_y)\, g_0(r)}_{\text{unperturbed distribution}} + \underbrace{f_1(J_y, \theta_y)\, g_1(z,\delta) \exp\left(\frac{j\Omega s}{v}\right)}_{\text{perturbation to be found}} . \tag{2.12}$$

Using polar coordinates $z = r\cos\phi$ and $\delta = \frac{\omega_s}{\eta v} r \sin\phi$, Vlasov's equation 2.11 will simplify as [14, p. 18]

$$\left(f_1 g_1 \frac{j\Omega s}{v} + \frac{Q_y}{R} g_1 \frac{\partial f_1}{\partial \theta_y} + \frac{\omega_s}{v} f_1 \frac{\partial g_1}{\partial \phi}\right) \exp\left(\frac{j\Omega s}{v}\right) = \frac{\sin\theta_y}{E} \sqrt{2 J_y \frac{R}{Q_{y0}}} F_y(z,s)\, g_0(r)\, f_0'(J_y) \,. \tag{2.13}$$

$f_1(J_y, \theta_y)$ can be expressed as $f(J_y)\exp(-j\theta_y)$ and $g_1(r,\phi)$ is Fourier expanded as [14, p. 22] [7, p. 295]

$$g_1(r,\phi) = \exp\left(-\frac{jQ_y' z}{\eta R}\right) \sum_{l=-\infty}^{l=+\infty} R_l(r) \exp(-jl\phi) \,, \tag{2.14}$$

leading to

$$\sum_{l=-\infty}^{l=+\infty} R_l(r) \exp(-jl\phi) \left(\frac{f(J_y)(Q_c - Q_{y0} - lQ_s)}{f_0'(J_y)\sqrt{2J_y \frac{R}{Q_{y0}}}}\right) = \frac{R}{2E} F_y(z,s) \exp\left(-j\frac{Q_c s}{R}\right) \exp\left(-j\frac{Q_y' z}{\eta R}\right) . \tag{2.15}$$

where $R_l(r)$ is the azimuthal mode l function.

The wake force $F_y(z,s)$ for a general impedance Z_y is proportional to [14, p. 33]

$$F_y(z,s) \propto \exp\left(j\frac{Q_c s}{R}\right)\sum_{l=-\infty}^{+\infty} j^{-l}\sum_{p=-\infty}^{+\infty}\exp\left(-j\left(Q_c+p\right)\frac{z}{R}\right)Z_y\left(-\omega_0\left(Q_c+p\right)\right) \tag{2.16}$$

$$\int_0^{\infty} rR_l(r)\,\mathrm{J}_l\left(\left(\omega_\xi-\omega_0\left(Q_c+p\right)\right)\frac{r}{v}\right)\mathrm{d}r\,, \tag{2.17}$$

and for an ideal damper treated as a single turn wake [14, p. 33] it is proportional to

$$F_y(z,s) \propto \exp\left(j\frac{Q_c s}{R}\right)\sum_{l=-\infty}^{+\infty} j^{-l}\int_0^{\infty} rR_l(r)\,\mathrm{J}_l\left(\frac{\omega_\xi r}{v}\right)\mathrm{d}r\,. \tag{2.18}$$

Combining equations 2.15, 2.17 and 2.18, integrating over ϕ and taking $\tau=\frac{r}{v}$ yields

$$\left(\Omega-Q_{y0}\omega_0-l\omega_s\right)R_l(\tau) \;=-\kappa g_0(\tau)\sum_{l'=-\infty}^{\infty} j^{l'-l}\int_0^{\infty}\mathrm{d}\tau'\tau' R_{l'}(\tau')\left(\overbrace{\frac{\mu}{\omega_0}\mathrm{J}_l\left(-\omega_\xi\tau\right)\mathrm{J}_{l'}\left(-\omega_\xi\tau'\right)}^{\text{damper term}}\right. \tag{2.19}$$

$$\left.+\underbrace{\sum_{p=-\infty}^{\infty} Z_y(\omega_p)\,\mathrm{J}_l\left(\left(\omega_\xi-\omega_p\right)\tau\right)\mathrm{J}_{l'}\left(\left(\omega_\xi-\omega_p\right)\tau'\right)}_{\text{impedance term}}\right). \tag{2.20}$$

Equation 2.20 is called Sacherer integral equation[9, p. 284]. It is an eigensystem as the radial function $R_l(\tau)$ taken for a certain azimuthal mode l is a function of all the radial functions.

2.3 Eigenvalues problem

In order to solve Sacherer integral equation 2.20, DELPHI performs a Discrete Expansion over Laguerre Polynomials of the integral. In the end, Sacherer integral equation will become a classical eigenvalue problem, which can be solved numerically.

The radial functions $g_0(\tau)$ and $R_l(\tau)$ are decomposed over Laguerre polynomials (the first polynomials are shown in figure 2.1) [14, p. 39]

$$R_l(\tau)=\left(\frac{\tau}{\tau_b}\right)^{|l|}\exp\left(-b\tau^2\right)\sum_{n=0}^{\infty} c_{n,l}\mathrm{L}_n^{|l|}\left(a\tau^2\right) \tag{2.21}$$

$$g_0(\tau)=\exp\left(-b\tau^2\right)\sum_{k=0}^{n_0} g_k\mathrm{L}_k^{0}\left(a\tau^2\right)\,. \tag{2.22}$$

After substituting equations 2.21 and 2.22 into 2.20 and integrating over τ, two integrals appear

$$\int_0^{\infty}\tau^{|l|+1}\exp\left(-a\tau^2\right)\mathrm{J}_l\left(\left(\omega_\xi-\omega_p\right)\tau\right)\mathrm{L}_k^{0}\left(a\tau^2\right)\mathrm{L}_n^{|l|}\left(a\tau^2\right)\mathrm{d}\tau \tag{2.23}$$

$$\int_0^{\infty}\tau^{|l|+1}\exp\left(-a\tau^2\right)\mathrm{J}_l\left(-\omega_\xi\tau\right)\mathrm{L}_k^{0}\left(a\tau^2\right)\mathrm{L}_n^{|l|}\left(a\tau^2\right)\mathrm{d}\tau\,. \tag{2.24}$$

These two integrals can be computed analytically [1, p. 43]

$$\int_0^{\infty}\tau^{|l|+1}\exp\left(-a\tau^2\right)\mathrm{J}_l\left(-\omega_\xi\tau\right)\mathrm{L}_k^{0}\left(a\tau^2\right)\mathrm{L}_n^{|l|}\left(a\tau^2\right)\mathrm{d}\tau=\frac{(-1)^{n+k+|l|}\,\omega_\xi^{|l|}}{(2a)^{|l|+1}}\mathrm{L}_k^{k-n}\left(\frac{\omega_\xi^2}{4a}\right)\mathrm{L}_n^{k-n+|l|}\left(\frac{\omega_\xi^2}{4a}\right)\,. \tag{2.25}$$

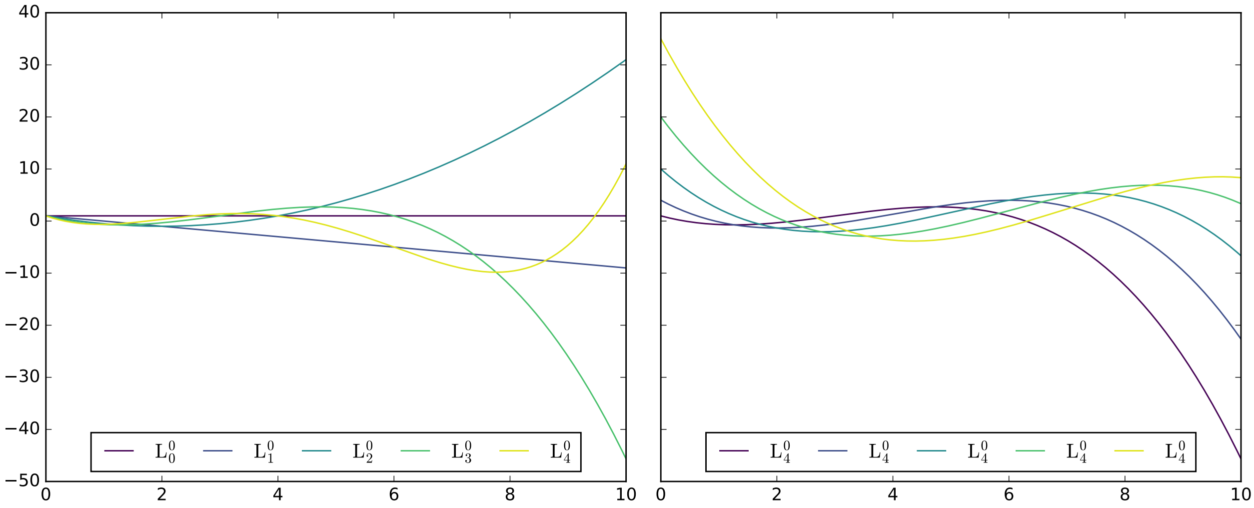

Figure 2.1: First Laguerre polynomials for $l = 0$ (left) and for $n = 3$ (right)

Sacherer integral equation 2.20 can then be written as an eigenvalue problem

$$(\Omega - Q_{y0}\omega_0)\, c_{n,l} = \sum_{l'=-\infty}^{\infty} \sum_{n'=0}^{\infty} c_{n',l'} \left(\delta_{l,l'} \delta_{n,n'} l \omega_s + \mathbf{M}_{l,n,l',n'} \right) , \tag{2.26}$$

where $\mathbf{M}$ is the combined impedance and damper matrix. The eigenvalues problem presents a two fold infinity with l the azimuthal mode number and n the radial mode number. When the problem is numerically solved, the matrix is truncated and only some modes are taken into account. In DELPHI, the maximum number of radial and azimuthal modes has been limited to 16 (from 0 to 15) and 33 (from -16 to 16) to limit computation time.

2.4 Signal created by the perturbation

The eigenvalues $(\Omega - Q_{y0})$ associated with each mode (n, l) are the frequency shift of this mode: the real part will represent by how much the tune shifts from the unperturbed value Q_{x0} and the imaginary part gives the growth rate of the perturbation associated with this mode. These two quantities can be computed for various input parameters such as impedance models, chromaticities,or bunch intensities. It is also a way to check and improve the impedance model of an accelerator as the tune shifts and growth rates can be measured on the machine.

On the other hand the eigenvector associated with mode (n, l) gives this mode spectrum. Once Fourier transformed, the spectrum gives the signal which can be observed with beam position monitors installed in the machine. Some oscillation patterns are represented in figure 2.2 and examples of mode spectra and signal are given in figure 2.3. In these plots, the horizontal axis of the plots on the first are in the frequency domain whereas the horizontal axis of the plots on the second and third rows are in the time domain and corresponds to the bunch longitudinal extension.

In DELPHI only the eigenvalues are currently used. The signal can be obtained from the eigenvectors by reconstructing the transverse perturbation $g_1(r, \phi)$. From [7, p. 296] the distribution spectrum $\tilde{\lambda}(\omega')$ can be written as

$$\tilde{\lambda}(\omega') = \frac{\omega_{s0}}{\eta c} \int_{r=0}^{r=+\infty} \int_{\phi=0}^{\phi=2\pi} r \exp\left(j \frac{\omega' r \cos\phi}{c} \right) g_1(r, \phi)\, \mathrm{d}r \mathrm{d}\phi\, , \tag{2.27}$$

where $\omega' = p\omega_0 + \Omega$ and $p \in \mathbb{Z}$. Inserting 2.21 in 2.27 yields

$$\tilde{\lambda}(\omega') = \frac{\omega_{s0}}{\eta c} \sum_{l=-\infty}^{+\infty} \int_{r=0}^{r=+\infty} r R_l(r)\, \mathrm{d}r \int_{\phi=0}^{\phi=2\pi} \exp\left(-jl\phi + j \left(\frac{\omega' r}{c} - \frac{Q' r}{\eta R} \right) \cos\phi \right) . \tag{2.28}$$

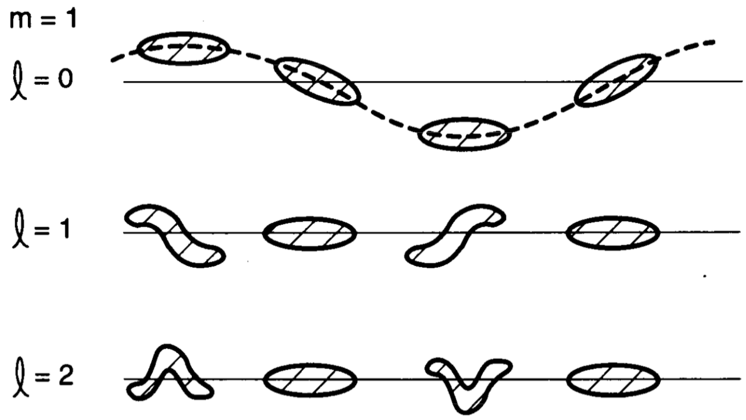

Figure 2.2: Sketch of the longitudinal structure of the beam executing transverse oscillations. Successive snapshots are represented for the first three azimuthal modes. Sketch from A. Chao [7]

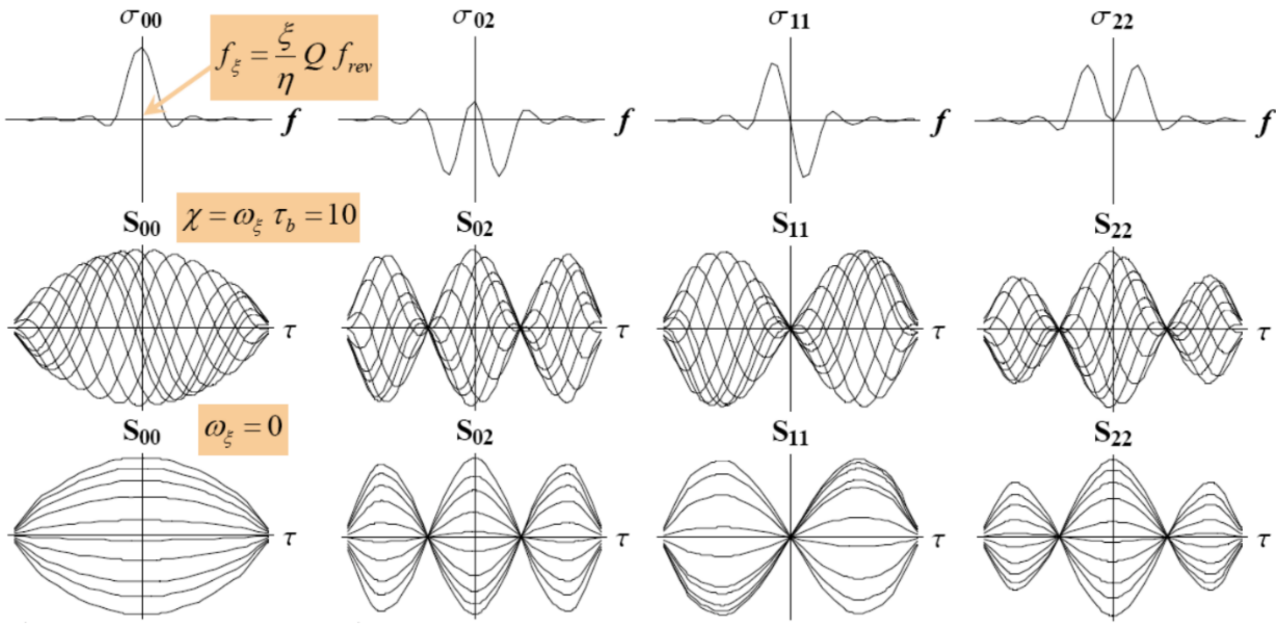

Figure 2.3: Spectrum of some oscillation modes (first row), and the associated signal that could be observed, with a positive chromaticity (second row) and without chromaticity (third row). Sketch from E.Métral [11]

With the relations from [7, p. 297]

$$\frac{1}{2\pi}\int_0^{2\pi} \exp\left(jl\phi - jx\cos\phi\right) \mathrm{d}\phi = j^{-l}\mathrm{J}_l\left(x\right) \tag{2.29}$$

$$\mathrm{J}_{-l}\left(x\right) = \mathrm{J}_l\left(-x\right) \ , \tag{2.30}$$

we get

$$\tilde{\lambda}\left(\omega'\right) = \frac{2\pi\omega_{s0}}{\eta c}\sum_{l=-\infty}^{+\infty} j^l \int_0^{+\infty} rR_l\left(r\right)\mathrm{J}_l\left(\frac{\omega' r}{c} - \frac{Q' r}{\eta R}\right)\mathrm{d}r \, . \tag{2.31}$$

From this formula the signal is reconstructed as follows:

1. an eigenvalue Ω is selected and its corresponding eigenvector is retrieved;
2. $R_l\left(\tau = \frac{r}{c}\right)$ from equation 2.21 is reconstructed for each value of l. The retrieved eigenvector gives the coefficient $c_{n,l}$ of the decomposition;
3. equation 2.31 is computed for a range of ω'.

The signal plotting with DELPHI is currently under development. Sample results obtained with a basic impedance model (resistive wall impedance described in section 3.1) are showed in figure 2.4. The horizontal axis graduation is in the order of the longitudinal bunch length but it still needs to be scaled properly.

The signal associated with the first eigenvalue given by DELPHI is showed. This eigenvalue corresponds to the most unstable mode which can develop itself. Plot 2.4a shows the signal associated with a mode 0 instability developing at negative chromaticity. Plot 2.4b shows the signal obtained for a positive chromaticity $Q' = 1$ where a mode -1 instability is developing.

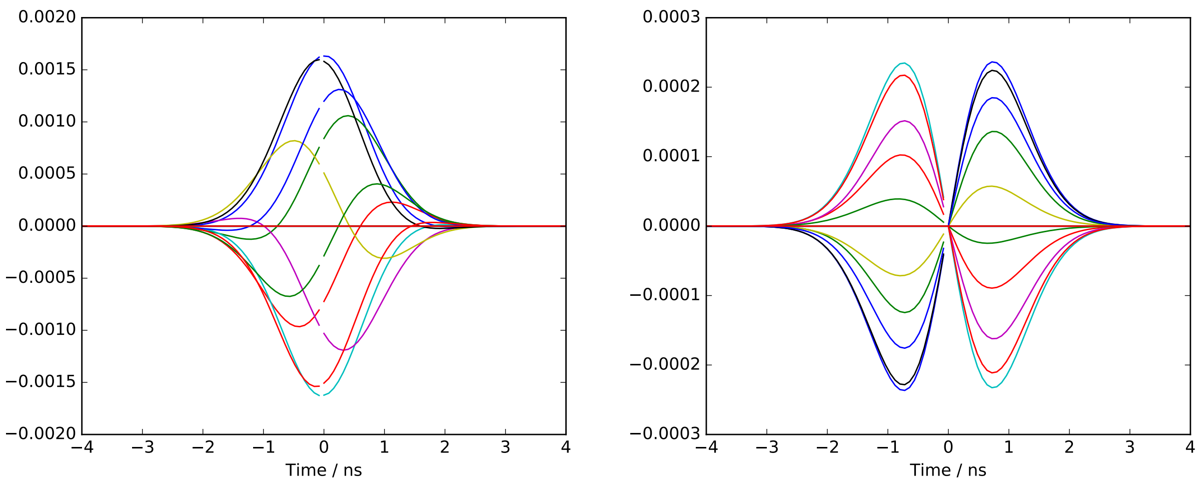

(a) DELPHI signal, chromaticity $Q' = -5$

(b) DELPHI signal, chromaticity $Q' = 1$

Figure 2.4: Example of signals obtained with DELPHI for a resistive wall impedance.

We saw that Vlasov equation formalism allows a fast determination of stability limits through the solving of an eigenvalues problem. The code DELPHI bases itself on this formalism and the treatment of its output, a system of eigenvalues and eigenvectors, enables us to determine the tune shifts and growth rates of the modes developing in the beam. The treatment of the eigenvectors will allow to obtain a measurement of the longitudinal beam profile as seen on beam positions monitors.

Chapter 3

Beam stability studies with DELPHI

This part will expose beam stability studies performed with DELPHI. At first simple models where used to apprehend the formalism used in the code and to compare the results with theoretical models. The Transverse Mode Coupling Instability (TMCI) was also studied for a simple impedance model and for the LHC as well. This instability was also studied for four FCC-hh impedance model which are also exposed. New longitudinal distributions have also been implemented in DELPHI to better match the real beam profile.

3.1 Basic studies with a resistive wall impedance

A simple case for the study of impedance effects on beam dynamics is the resistive wall. The beam is surrounded by a thick pipe of radius b. The resistive wall impedance can be written [9, p. 310]:

$$Z_{\perp,RW}\left(\omega\right) = \left(1+j\right)\frac{R}{b^3}Z_0\delta_0\sqrt{\frac{\omega_0}{\omega}}$$

where R is the machine radius, $Z_0 = 377\,\Omega$ the free space impedance and δ the skin depth taken at the revolution frequency ω_0. This model assumes that the skin depth δ is lower than the beam pipe thickness. In an accelerator, the beam pipe is a main contributor to the resistive wall impedance as it is the longest element seen by the beam.

3.1.1 Resistive wall model

The beam pipe model used in this section is pictured in figure 3.1 and both beam and beam pipe parameters are given in table 3.1. The beam parameters are taken from the LHC at 450 GeV, its injection energy. The impedance model is computed with Impedance Wake 2D (IW2D), a code which performs analytical computations of wakefields and impedance using a point charge beam. This allows to perform fast impedance calculations, as opposed to numerical simulations which give a more precise model at the cost of a longer computation time. The resulting impedance model is showed in figure 3.2.

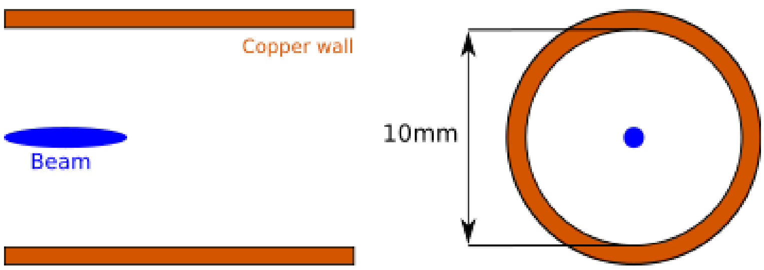

Figure 3.1: Beam pipe model used in the resistive wall impedance simulations.

Beam parameter	Value
Beam energy / GeV	450
γ factor	479.6
Bunch intensity / protons	1×10^{11}
Number of bunches	1
RMS bunch length σ_z / m	0.1124
4 RMS bunch length / ns	1.5
Horizontal tune Q_x	64.31
Vertical tune Q_y	59.32
Synchrotron tune Q_s	4.905×10^{-3}
Resistive wall parameter	**Value**
Revolution frequency / Hz	11 245.5
Machine circumference / m	26 659
Pipe radius / mm	5
Material	Copper at 300 K
Skin depth at 11 kHz / µm	618.8

Table 3.1: Beam parameters and beam pipe model used for the resistive wall study.

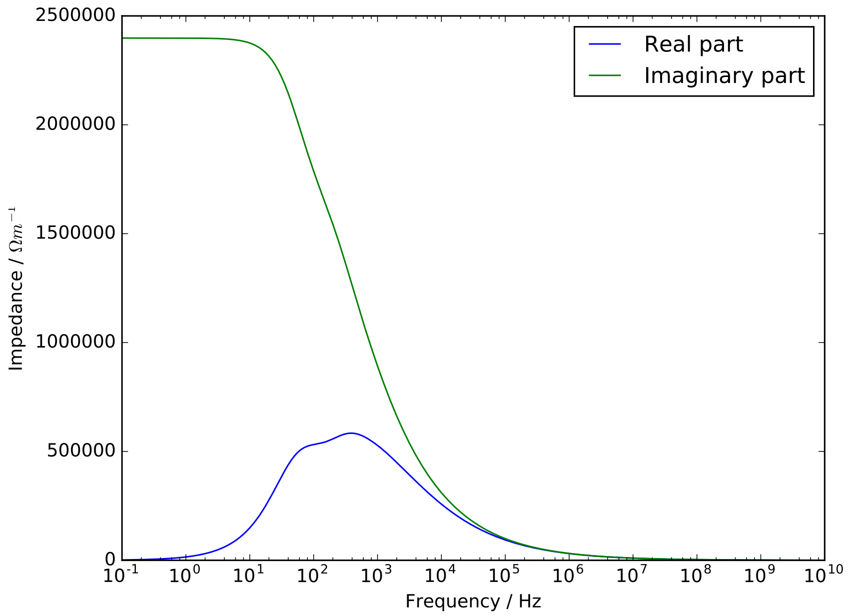

Figure 3.2: Horizontal dipolar impedance as a function of frequency for the resistive wall model described in table 3.1.

3.1.2 Chromaticity scan

In this first DELPHI study with the resistive wall impedance model the machine chromaticity $Q' = Q_0\xi$ (also denoted Q_p in the plots) is scanned from -10 to 20 by steps of 1 unit. For each value of chromaticity, DELPHI gives a set of eigenvalues $\Omega - Q_{y0}\omega_0 - l\omega_s$ with l the mode number, as described by equation 2.26. The real part of this complex number gives the tune shift and the imaginary part gives the growth rate of the perturbation. A positive growth rate means that the perturbation will increase, the mode is unstable. A negative growth rate means that the perturbation is damped, the mode is stable.

In figure 3.3 the most unstable mode tune shift is plotted as a function of the chromaticity for the horizontal plane. The tune shift

$$\frac{\Re\left(\Delta Q_x\right)}{Q_s} = \frac{1}{Q_s}\left(\frac{\Omega}{\omega_0} - Q_{y0} - l\right) \tag{3.1}$$

normalized to the synchrotron tune Q_s tells by how much the unperturbed tune Q_{y0} is shifted because of the impedance effects. The most unstable mode is the one with the largest imaginary part.

For the resistive wall impedance case, the theory [7, pp. 349-352][9, p.317] indicates that above transition ($\eta \geq 0$), a negative chromaticity will drive a mode 0 instability. For positive chromaticity, mode 0 is stable but higher order modes appear: mode 1 first then mode 2. However these higher order modes are more difficult to drive and their growth rates are lower.

This simple result indicates that for a machine operating above transition such as the SPS or the LHC, a positive chromaticity is needed. In fact the natural chromaticity of the machine is negative thus sextupoles magnets are introduced in the machine lattice to correct it.

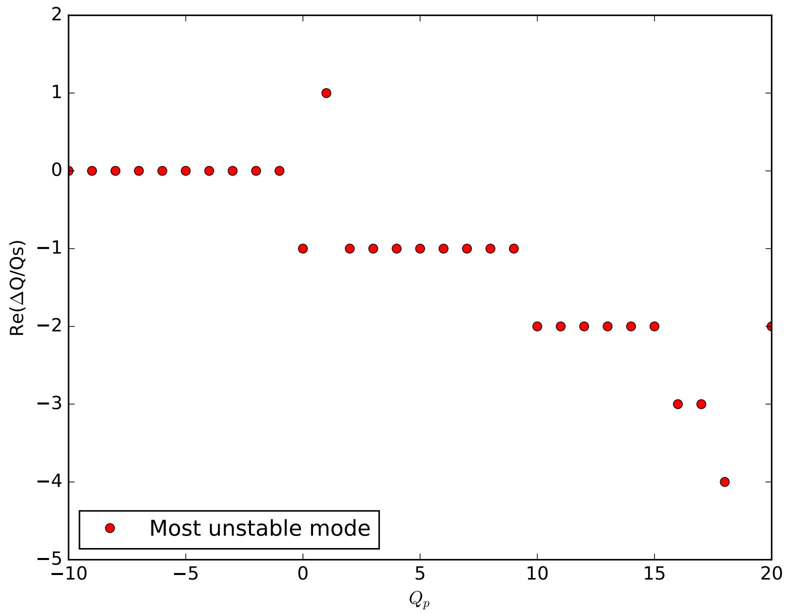

Figure 3.3: Most unstable mode tuneshift for a resistive wall impedance, as a function of chromaticity.

3.2 Effect of the longitudinal distribution

In DELPHI the longitudinal particle distribution is written as a finite sum of Laguerre polynomials (equation 2.22). This allows to implement multiple distributions to better fit the actual beam profile present in the machine or to compare simulations results with examples developed in the literature.

3.2.1 Implementation of different longitudinal distributions in DELPHI

The longitudinal particle distribution $g_0(\tau)$ is decomposed over Laguerre polynomials as follows:

$$g_0(\tau) = \exp\left(-b\tau^2\right) \sum_{k=0}^{n_0} g_k \mathrm{L}_k^0 \left(a\tau^2\right) \tag{3.2}$$

where a and b are parameters chosen by the user and τ_b is the half bunch length.

Only the Gaussian distribution was implemented in DELPHI. In this case the decomposition over Laguerre polynomials is reduced to one term, as $\mathrm{L}_k^0(a\tau^2) = 1$

$$g_0(\tau) = \exp\left(-b\tau^2\right) \mathrm{L}_k^0\left(a\tau^2\right) = \exp\left(-b\tau^2\right) . \tag{3.3}$$

In DELPHI the distribution is normalized with respect to the full bunch length τ_b, which is taken equal to 4 standard deviations in the Gaussian case. Because of the symmetry, the distribution is written for positive values of τ only. Taking $a = b = 8$, the Gaussian distribution can be written

$$g_0(\tau) = \frac{8}{\pi\tau_b^2} \exp\left(-8\left(\frac{\tau}{\tau_b}\right)^2\right), \tau \in [0; +\infty[. \tag{3.4}$$

Three other distributions have been implemented in DELPHI: the parabolic amplitude, the parabolic line and the uniform distribution. Their respective equations are

$$g_0(\tau) = \frac{8}{\pi\tau_b^2}\left(1 - \left(\frac{2\tau}{\tau_b}\right)^2\right), \tau \in \left[0; \frac{\tau_b}{2}\right] \tag{3.5}$$

$$g_0(\tau) = \frac{6}{\pi\tau_b^2}\sqrt{1 - \left(\frac{2\tau}{\tau_b}\right)^2}, \tau \in \left[0; \frac{\tau_b}{2}\right] \tag{3.6}$$

$$g_0(\tau) = \frac{4}{\pi\tau_b^2} \frac{1}{1 + \exp\left(\frac{25}{\tau_b}\left(\tau - \frac{\tau_b}{2}\right)\right)}, \tau \in [0; +\infty[. \tag{3.7}$$

The uniform distribution is approximated by a sigmoid function for convergence reasons: the decomposition being done with continuous functions, a discontinuity in the longitudinal distribution would require a higher number of terms in the Laguerre decomposition to reach the convergence criterion, thus making DELPHI's calculations longer.

The different distributions and the corresponding decompositions are shown in figure 3.4.

3.2.2 Comparison of DELPHI's results with analytical predictions

In order to check that the new distributions are correctly implemented, a comparison of DELPHI's results is made with analytical formulas. The impedance model used in DELPHI is the one from the SPS. The beam stability is computed in the horizontal x plane. A scan in intensity is performed for a fixed chromaticity of $Q' = -3$. The tuneshift of the most unstable mode is plotted in figure 3.5. For each distribution a linear fit is performed, whose results are given in table 3.2.

These results are compared with analytical formulas from [3, p. 57], which states that the tuneshift ΔQ_x caused by a general impedance at zero chromaticity is proportional to

$$\Delta Q_x \propto \frac{\int_{-\infty}^{+\infty} g_0(\tau)^2 \, \mathrm{d}\tau}{\left(\int_{-\infty}^{+\infty} g_0(\tau) \, \mathrm{d}\tau\right)^2} . \tag{3.8}$$

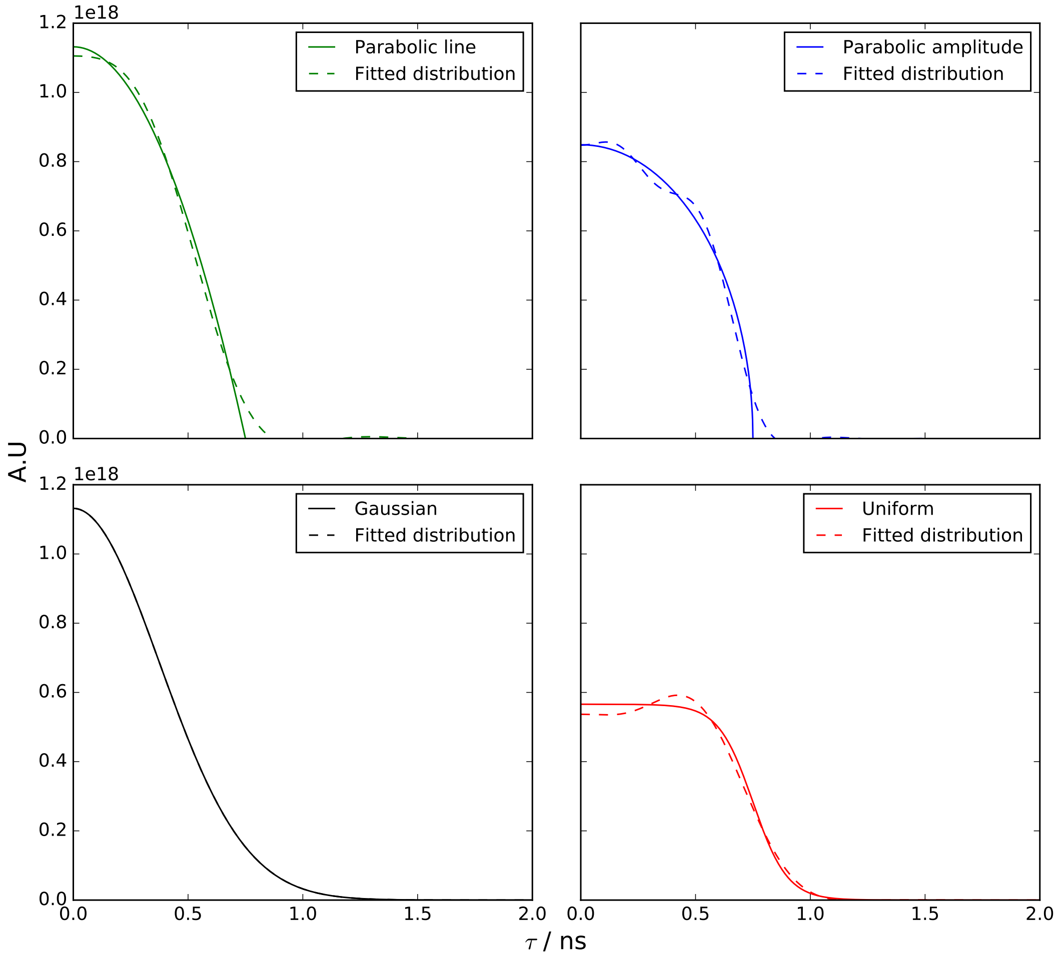

Figure 3.4: The different longitudinal distributions used in DELPHI and their expression in terms of Laguerre polynomials.

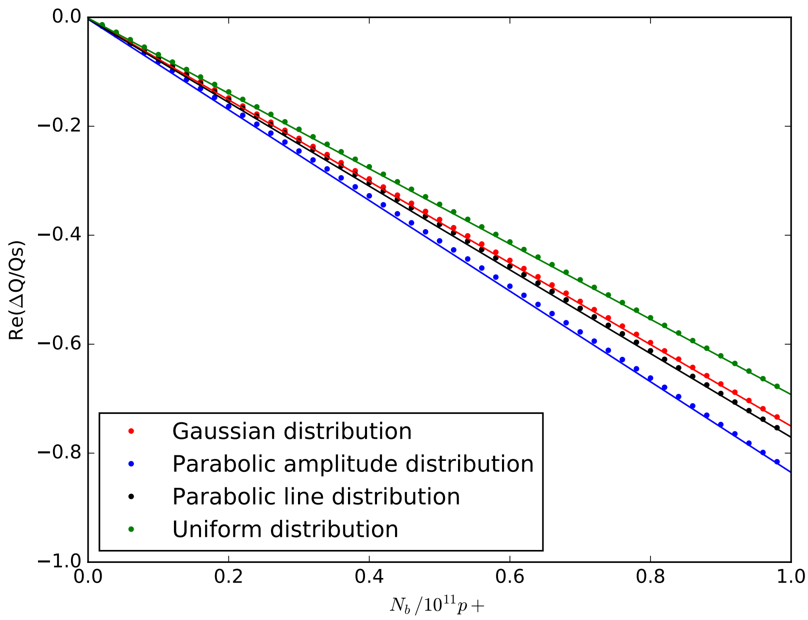

Figure 3.5: Most unstable mode tuneshift for different longitudinal distributions. Scan on bunch intensity for chromaticity $Q' = -3$. Results obtained with DELPHI and linear fitting.

Case	Linear fit equation
Gaussian	$y = -0.659x + 0.004$
Parabolic amplitude	$y = -0.772x + 0.002$
Parabolic line	$y = -0.640x + 0.004$
Uniform	$y = -0.537x + 0.004$

Table 3.2: Equations of the linear fit performed on mode 0 tuneshift for the different distributions.

Formula 3.8 yields for the various distributions:

$$\Delta Q_x|_{\text{gaussian}} \propto \frac{4}{\pi^{\frac{1}{2}}\tau_b} \tag{3.9}$$

$$\Delta Q_x|_{\text{parabolic amplitude}} \propto \frac{12}{5\tau_b} \tag{3.10}$$

$$\Delta Q_x|_{\text{parabolic line}} \propto \frac{64}{3\pi^2\tau_b} \tag{3.11}$$

$$\Delta Q_x|_{\text{uniform}} \propto \frac{2}{\tau_b}\,. \tag{3.12}$$

First, the ratio between the slopes from table 3.2 is performed. Then the corresponding tuneshift ratio is performed from the analytical calculations above. The results are shown in table 3.3. A good agreement is found between the theory and the simulations, considering that the distributions in DELPHI are approximated with Laguerre polynomials. The simulations data are also retrieved for a slightly negative chromaticity so that mode 0 is the most unstable mode: discrepancies from the analytical model may also arise from this.

The implementation of these new longitudinal distributions in DELPHI will allow to better fit other machines parameters and also simulations with theoretical models which often base themselves on simple distributions such as the Gaussian one.

Ratio	From linear fit	From analytical calculations
Uniform/Gaussian	0.816	0.886
Parabolic amplitude/Gaussian	1.17	1.06
Parabolic line/Gaussian	0.971	0.958

Table 3.3: Comparison of the ratio of the linear fits slopes versus analytical predictions.

3.3 TMCI studies

The Transverse Mode Coupling Instability (TMCI) is a coherent instability mechanism arising as the beam intensity increases. First the instability mechanism is explained and then DELPHI simulations are performed with a basic impedance model and with the LHC impedance model.

3.3.1 Transverse Mode Coupling Instability

This instability occurs when the beam intensity increases: as the tune shift of a mode increases with the beam intensity, it can encounter and couple with a higher order mode. The top plot of figure 3.6

depicts such a case: the mode $l = 0$ line shifts downward as the intensity increases. It encounters the mode $l = -1$ line at a 1×10^{12} protons per bunch intensity. The bottom plot of figure 3.6 shows that once mode 0 reaches mode -1 a positive growth rate appears: the mode becomes unstable.

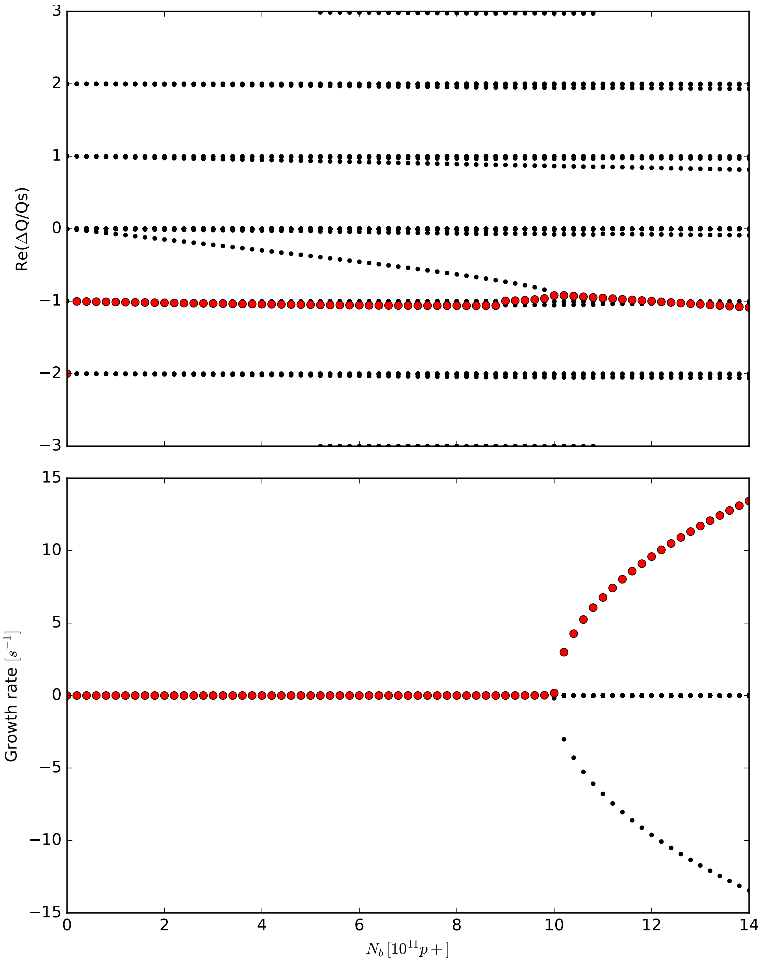

Figure 3.6: Mode shifts (top) and growth rates (bottom) versus bunch intensity (in protons per bunch) obtained with DELPHI simulations for an FCC-hh impedance model, described in section 3.4.2. Red points indicate the most unstable mode (eigenvalue with the largest imaginary part).

3.3.2 Purely inductive impedance

The TMCI mechanism can be explained in terms of forces acting on the beam [9, p. 296]. In our model, these forces are driven by the machine's impedance (see section 1.2). As in electrical theory, the impedance has an imaginary part (inductive or capacitive impedance) and a real part (resistive impedance).

If the impedance is purely inductive (positive imaginary part and no real resistive part), the growth rates of the different modes are equal to zero. This result can be derived with Sacherer theory from [16]: at low beam intensity, the complex tune shift of a mode is proportional to the transverse effective impedance of the considered mode $Z_{\perp n,l}$

$$\Delta Q \propto jZ_{\perp n,l} = j\frac{\int_{-\infty}^{-\infty} h_{n,l}\left(\omega\right) Z_{\perp}\left(\omega\right)}{\int_{-\infty}^{-\infty} h_{n,l}\left(\omega\right)}\,, \tag{3.13}$$

where $h_{n,l}$ is the beam frequency spectrum (see figure 3.15). In the case of constant inductive impedance, the effective impedance $Z_{\perp n,l}$ is a pure imaginary number thus the tune shift is a real number as equation 3.13 shows. The absence of an imaginary part means that the mode can not become unstable.

The constant inductive impedance model given as a DELPHI input is in fact a broadband resonator with a very high resonance frequency as showed in table 3.4. The real part of the impedance is not strictly equal to zero but is much lower than the inductive part as plot 3.7 indicates.

Parameter	Horizontal plane x
Resonance frequency / GHz	1×10^6
Shunt impedance / $\mathrm{M\Omega \cdot m^{-1}}$	10
Quality factor	1

Table 3.4: Broadband resonator parameters for the constant inductive impedance model.

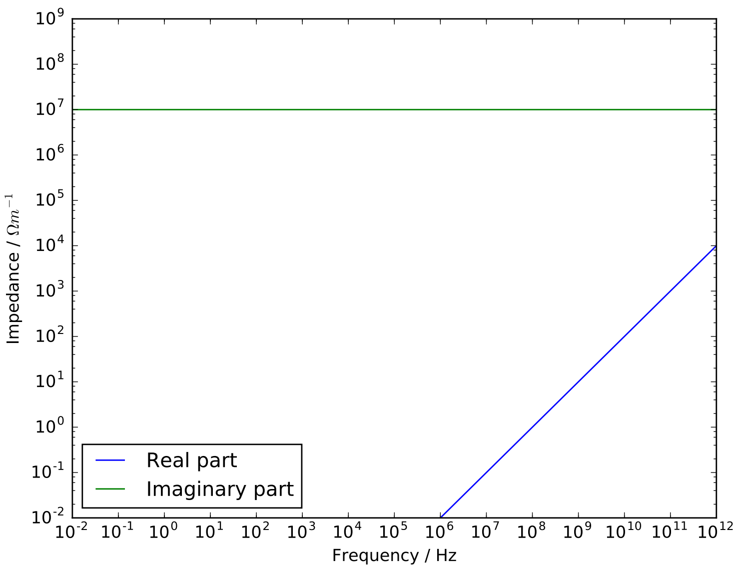

Figure 3.7: Broadband resonator impedance model used to simulate a constant inductive impedance.

The results obtained with DELPHI are compared to the one obtained by Elias Métral for a constant inductive impedance using the model of a beam with a constant longitudinal distribution of particles. In this case the eigenvalues problem derived from Vlasov equation is easier to solve with computer algebra systems such as Mathematica. Figure 3.8 shows the results given by the two methods. In this plot the horizontal axis is scaled to the tune shift of mode $(0, 0)$ as

$$\frac{\Delta Q_{coh}}{Q_s} = N_b \frac{e^2 Z_{\perp 0,0}}{4\pi\gamma m_p c Q_x \tau_b \omega_s}, \tag{3.14}$$

where $e = 1.6 \times 10^{-19}\,\mathrm{C}$ is the elementary charge, τ_b is the total bunch length, taken equal to 4 RMS bunch length σ_z for a Gaussian beam. This normalization allows to compare simulations using different impedance models or machine parameters.

The agreement between the two simulations is excellent for the mode $l = +1$ having the largest shift. It is good for modes $l = 0$, $l = -1$ and $l = -2$ until $\Delta Q_{coh}/Q_s \approx 1.5$. Discrepancies are observed for higher intensities and for modes $l = -3$. These discrepancies may come from the different longitudinal distributions used in the two computations. New simulations with DELPHI will be conducted with a uniform longitudinal distribution as to have more consistent results.

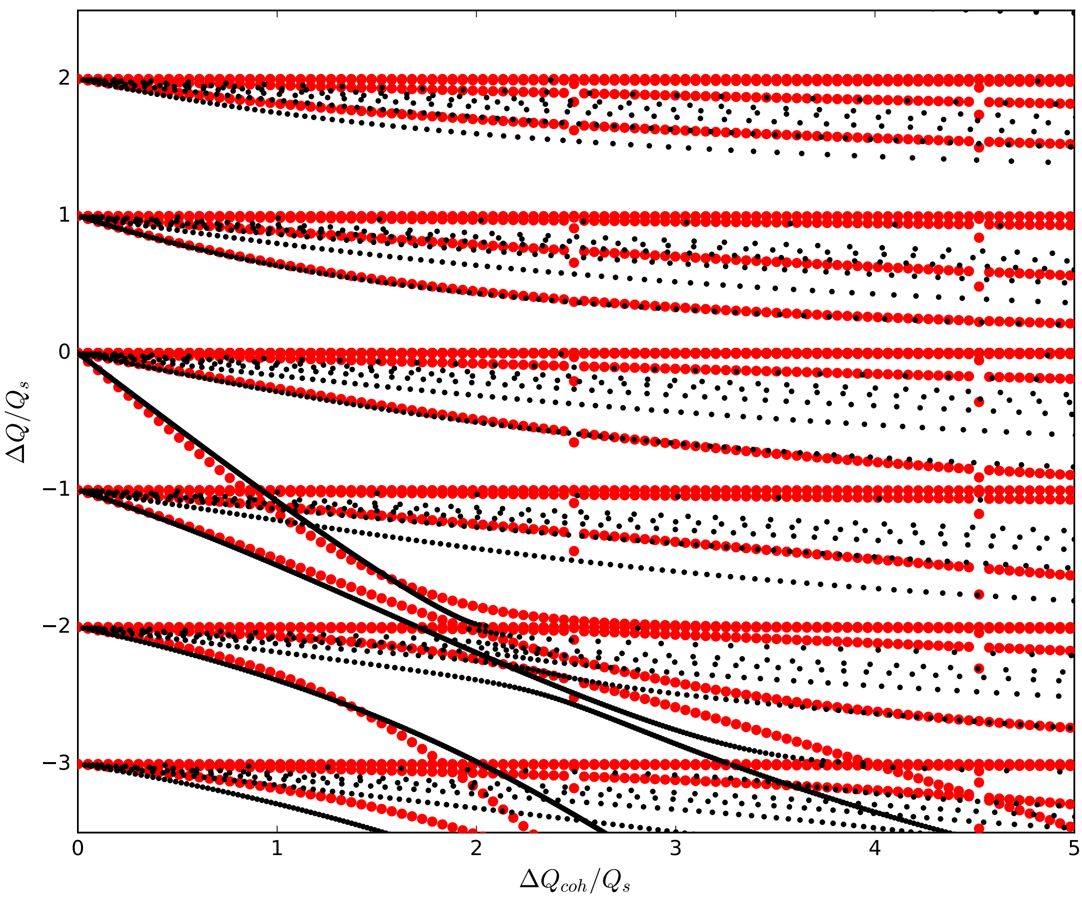

Figure 3.8: Tune shifts obtained with an inductive impedance. In red DELPHI results with a Gaussian beam. In black Elias Métral eigenvalues obtained for a uniform longitudinal distribution [12].

3.3.3 LHC at injection

In the LHC, the TMCI is more critical at injection energy (450 GeV) since the tune shifts are higher: the intensity threshold at which mode 0 and mode -1 will merge is lower than at top energy (6.5 TeV). This threshold has not been measured yet in the machine. DELPHI simulations were carried out to evaluate it for different chromaticities and bunch intensities.

Figure 3.9 shows the most unstable mode growth rate as a function of bunch intensity and chromaticity. We see that for negative chromaticity fast instabilities appear at an intensity threshold of about 2×10^{11} p.p.b. This corresponds to a mode 0 instability without mode coupling. At zero chromaticity a first instability appears at 8×10^{11} ppb and disappears at 11×10^{11} p.p.b: this corresponds to mode 0 and -1 coupling and then decoupling as the intensity increases. A new instability appears at 11×10^{11} p.p.b corresponding to mode -1 getting unstable without mode coupling. For positive chromaticities, the instability threshold is much higher (about 10×10^{11} p.p.b) because higher order modes are responsible for the instabilities and these modes are more difficult to drive.

These results show that with nominal machine parameters at injection the instability threshold is too high to be measured at zero chromaticity, the single bunch intensity limit in the LHC being around 2×10^{11} protons. Increasing the impedance by closing the collimators (whose purpose is described in section 3.4.2) might lower the intensity at which the TMCI appears, making it observable in the machine.

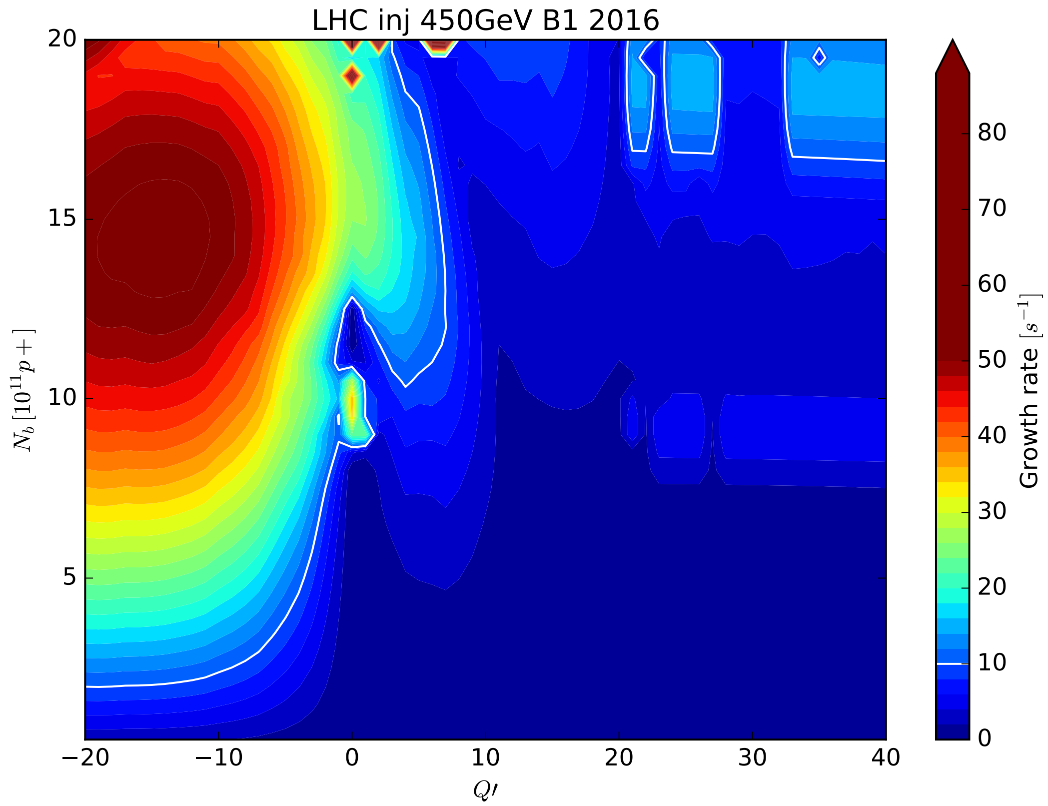

Figure 3.9: Growth rate of the most unstable mode as a function of the chromaticity and bunch intensity for the LHC at injection energy.

3.4 FCC-hh impedance model and beam stability

As some initial parameters for the FCC-hh collider have been proposed, it is possible to estimate the TMCI intensity threshold to assess the possible limitations of the machine with respect to collective effects. This part will first expose the impedance computations made and the stability thresholds obtained with these models.

3.4.1 Accelerator parameters and main components

Some parameters were given in table 1 and are recalled in table 3.5, where material parameters for the beam screen and the collimators are also indicated.

In the LHC and the FCC-hh project, the beam screen, pictured figure 3.10, is the copper coated pipe in which the beam circulates. The contribution of the beam screen on the impedance is mainly a resistive wall part as described in section 3.1.

The collimators are devices used to clean the particle halo surrounding the beam. If not scraped by the collimators, the halo would be lost in the main magnets of the machine provoking quenches. For the LHC, a quench of a superconducting magnet would happen for an energy deposition of $30\,\mathrm{mJ}\cdot\mathrm{cm}^{-3}$, corresponding to a local loss of 4×10^{7} protons. A single LHC bunch containing 1×10^{11} protons, and the machine being filled with about 2000 bunches, the collimation system is crucial for the machine operation.

In order to clean the beam halo, most of the collimators consists in a pair of movable jaws made of materials such as graphite or tungsten. In order to fulfil their purpose, the jaws have to be moved close to the beam. For some LHC collimators, the gap between two jaws can be as low as about 1 mm. Because of their proximity with the beam and the materials they are made of, the collimators contribution to the impedance is very high as we will see in section 3.4.2.

An other part of the accelerator taken into account are the interconnections between magnets. Their model has been studied by D.Ferrazza in [8] and is pictured figure 3.12. About 4000 of them would be present in the FCChh.

(a) LHC beam screen

(b) FCC-hh prototype beam screen

Figure 3.10: Pictures of the LHC and FCC-hh beam screens.

3.4.2 Impedance model for FCC-hh

A first impedance model for the FCC-hh was done by Xavier Buffat [6]. This model takes into account the beam pipe impedance as well as the collimators impedance. As showed in equation 3.1, the impedance caused by a resistive wall $Z_{\perp,RW}$ is proportional to:

$$Z_{\perp,RW} \propto \frac{1}{b^3} \tag{3.15}$$

Accelerator parameter at injection energy	Value
Beam energy / GeV	3000
γ factor	3197
Bunch intensity / protons	1×10^{11}
Number of bunches	10 600
RMS bunch length σ_z / m	0.08
4 RMS bunch length / ns	1.067
Horizontal tune Q_x	120.31
Vertical tune Q_y	120.32
Synchrotron tune Q_s	2.750×10^{-3}
Revolution frequency / Hz	2942.1
Beam screen properties	**Value**
Machine circumference / m	101 898.2
Beam screen radius / mm	13
Material	Copper at 50 K
Collimators properties	**Value**
Total length / m	17.8
Half gap / mm	(0.96–2.3)
Material	C, MoGr, W
Interconnects properties	**Value**
Length / m	1.36
Radius / mm	(0.96–2.3)
Material	Copper

Table 3.5: FCC-hh main parameters used in the studies.

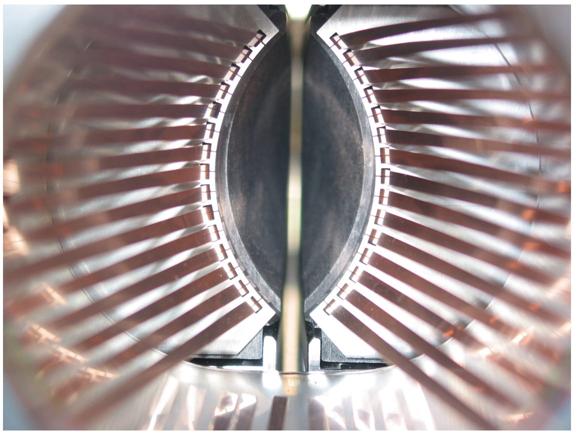

(a) View along beam path

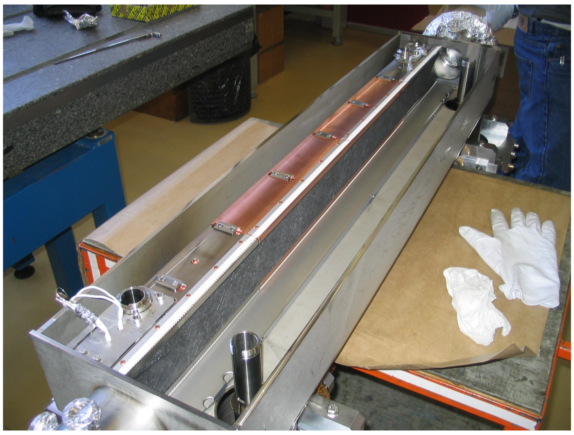

(b) Top view, only one jaw installed

Figure 3.11: Pictures of a LHC collimator.

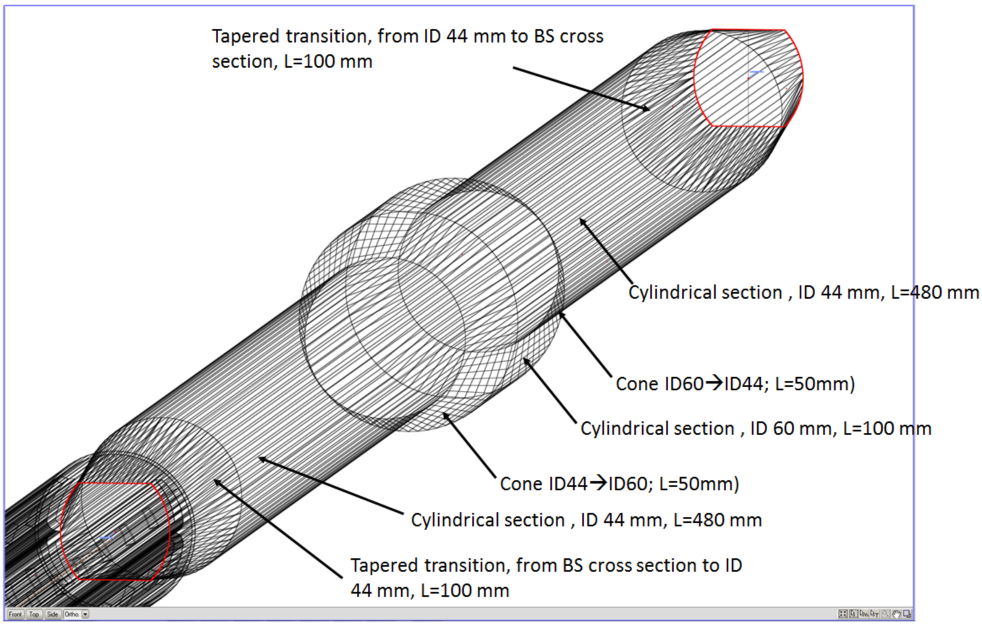

Figure 3.12: Interconnections model for the FCChh, from [8].

where b is the beam pipe radius. In the FCC study case, b is taken equal to 13 mm for the beam screen. For the collimators, b is the half gap between two jaws and is scaled from the LHC collimator model.

Because of their proximity with the beam, the collimators are a major contributor to the total impedance of the machine. The resulting impedance computed with Impedance Wake 2D for four basic models of FCChh are showed in figures 3.13 and 3.14. The four cases are:

- The beam screen only, consisting of an round pipe of 13 mm radius made of copper, labeled Beam Screen only
- The beam screen and the collimators, scaled from the LHC collimator model. These collimators are in graphite and tungsten. The simulation is labeled BS + C collimators
- The beam screen and the collimators, scaled from the HL-LHC collimator model. These collimators are in Molybdenum-Graphite (MoGr) and tungsten. MoGr collimators will be implemented to reduce the impedance among other [2]. The simulation is labeled BS + MoGr collimators
- The beam screen, the collimators scaled from the HL-LHC collimator model and the interconnects.

The whole interconnects are modelled as single resonator whose characteristics are given in table 3.6. Only the first resonance created by the interconnects at 3.05 GHz is modelled in this first approach.

Parameter	Horizontal plane x	Vertical plane y
Resonance frequency / GHz	3.05	3.05
Shunt impedance / $\mathrm{G}\Omega \cdot \mathrm{m}^{-1}$	173.60	277.77
Quality factor	86 801	

Table 3.6: Resonator parameters for the FCC-hh interconnects model.

The resulting transverse impedances are shown in figure 3.13 for the horizontal plane and in figure 3.14 for the vertical plane. We see the effect of the collimators on the impedance for frequencies higher than 1 kHz. The effect of the Molybdenum Graphite collimators on the impedance is clearly visible with a factor 3 gain. The impedance in the horizontal plane being slightly higher, the beam instability studies will be performed for this plane.

Having these impedance models, we compute the effective impedance Z_{eff}. This value is useful to derive a first estimation of the tune shifts caused by the impedance. We have [6]

$$Z_{eff0,0} = \frac{\int_{-\infty}^{-\infty} h_{0,0}\left(\omega\right) Z_{\perp}\left(\omega\right)}{\int_{-\infty}^{-\infty} h_{0,0}\left(\omega\right)}\,, \tag{3.16}$$

where $h_{0,0}\left(\omega\right)$ is the beam spectrum for the mode $n = l = 0$, represented in figure 3.15 and taken as in [15]

$$h_{00}\left(\omega\right) = \frac{4}{\pi^2} \frac{1 + \cos\left(\omega\tau_b\right)}{\left(\left(\omega\tau_b/\pi\right)^2 - 1\right)^2}\,. \tag{3.17}$$

In fact the effective impedance computed above is the one corresponding to the mode $n = l = 0$. For other modes the beam spectrum is different so the effective impedance is different. However mode 0 is often the most critical at negative chromaticity and computing the effective impedance for this case is an interesting first step. The results for the four study cases are presented in table 3.7. As expected the collimators have a significant contribution to the impedance budget of the machine.

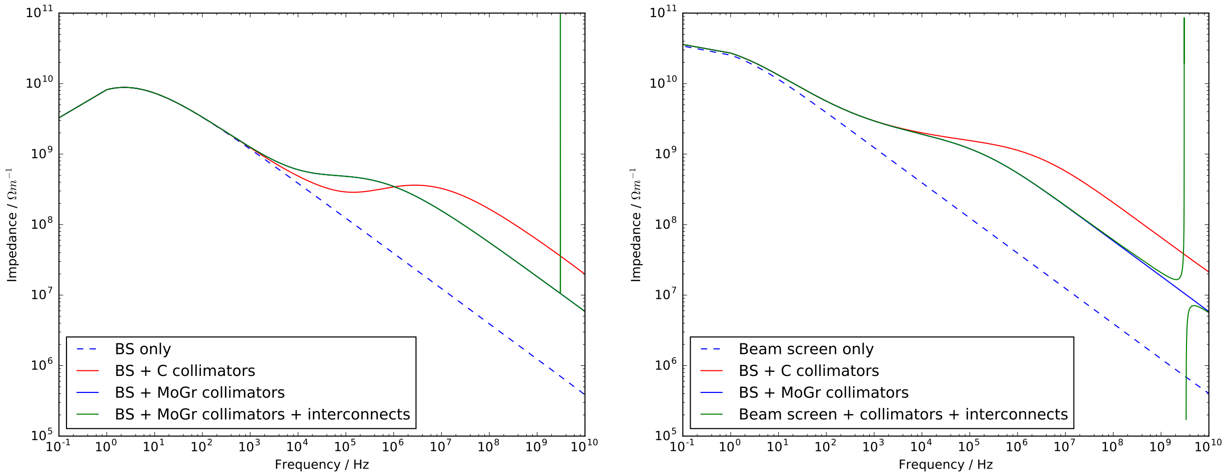

(a) Real part (b) Imaginary part

Figure 3.13: Transverse dipolar impedance in the horizontal plane as a function of frequency for four study cases of FCC-hh.

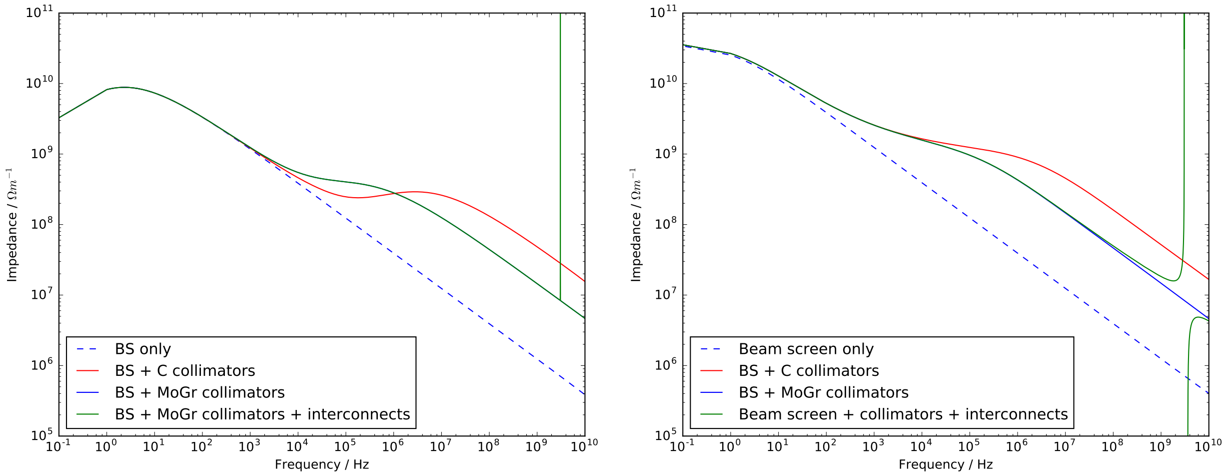

(a) Real part (b) Imaginary part

Figure 3.14: Transverse dipolar impedance in the vertical plane as a function of frequency for four study cases of FCC-hh.

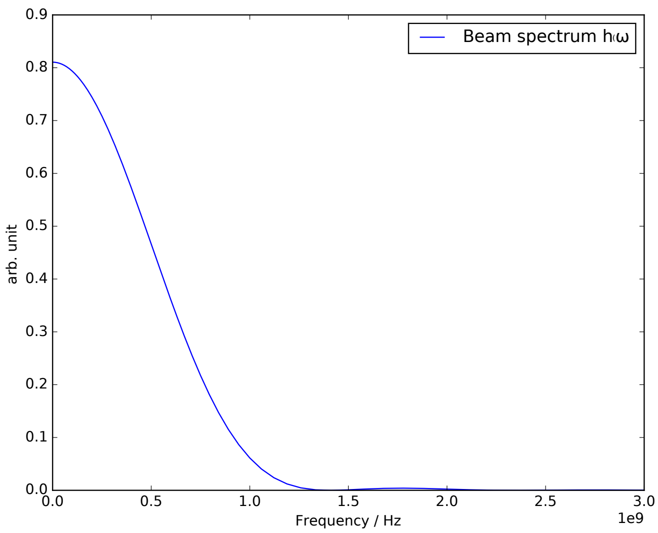

Figure 3.15: Beam spectrum $h(\omega)$ as a function of frequency used for the computation of Z_{eff}.

Case	Effective impedance (imaginary part) / $\mathrm{M\Omega \cdot m^{-1}}$
Beam screen only	3.15
Beam screen + graphite collimators	155.5
Beam screen + Molybdenum-Graphite collimators	46.4
Beam screen + Molybdenum-Graphite collimators + interconnects	48.4

Table 3.7: Imaginary part of the effective impedance for the four FCChh cases studied.

The effective impedance allows to approximate the coherent tune shift of mode 0 $\Delta Q_{c,x00}$ using Sacherer formula [16]:

$$\Delta Q_{c,x00} = j \frac{e^2 \beta N_b}{4\pi m_p \gamma Q_{x0} \omega_0 L_b} Z_{eff} \tag{3.18}$$

where $\beta = \frac{v}{c} \approx 1$, $e = 1.6 \times 10^{-19}$ C is the elementary charge, N_b is the number of protons in bunch and L_b is the total bunch length, taken equal to 4 RMS bunch length σ_z for a Gaussian beam.

In order to have a rough approximation of the TMCI threshold, one can compute the intensity N_b needed for the mode 0 to reach $-Q_s = -2.750 \times 10^{-3}$ with Sacherer formula 3.18. The approximate thresholds for the four study cases computes with this method are given in table 3.8. These results will be compared to the one obtained with DELPHI simulations in the next section.

Case	TMCI threshold / protons per bunch
Beam screen only	1.6×10^{12}
Beam screen + graphite collimators	3.3×10^{10}
Beam screen + Molybdenum-Graphite collimators	1.10×10^{11}
Beam screen + Molybdenum-Graphite collimators + interconnects	1.06×10^{11}

Table 3.8: TMCI threshold estimated with Sacherer formula for the FCChh study cases.

3.4.3 Stability studies with DELPHI

Having the impedance models allows to perform DELPHI simulations for the four cases studied. These simulations were performed for a chromaticity ranging from $Q_p = -20$ to 20, with an intensity scan depending on the studied case. The tune shifts and growth rates of the modes computed with DELPHI for 0 chromaticity are showed in figure 3.16 and figure 3.17. These plots allow to see the shift of mode 0 and at which intensity it crosses mode -1. The resulting values are given in table 3.9 and are compared with Sacherer formula predictions from equation 3.18 and table 3.8.

The results obtained with DELPHI are of the same order of magnitude as the one obtained with Sacherer formula. The agreement is within 30% for the three cases with collimators. For the beam screen only case, the agreement between DELPHI and Sacherer formula is poorer: this is due to the fact that Sacherer formula does not take into account the influence of other modes on the shift

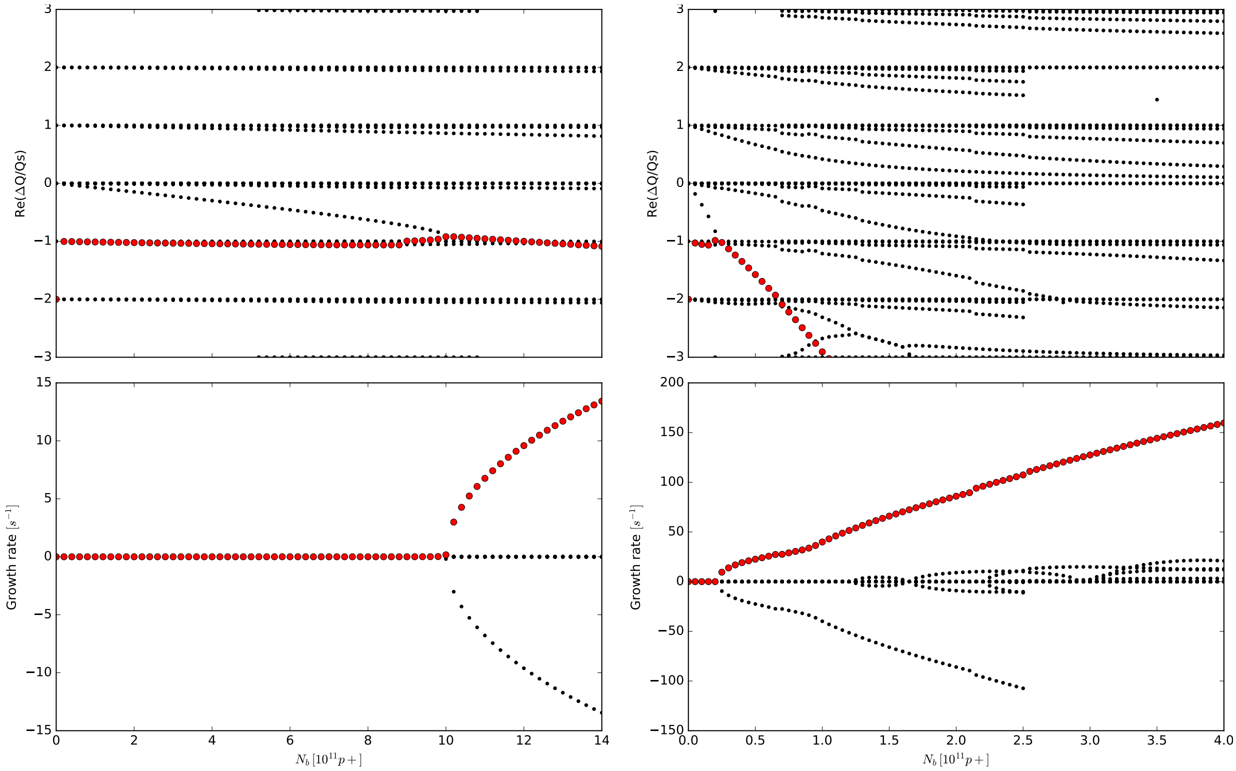

(a) Beam screen only

(b) BS + C collimators

Figure 3.16: Tune shifts and growth rates versus bunch intensity obtained with DELPHI simulations for the cases Beam screen only and Beam screen + graphite collimators. Red points signal the most unstable mode (eigenvalue with the largest imaginary part).

Case	TMCI threshold / protons per bunch	
	DELPHI	Sacherer
Beam screen only	1.0×10^{12}	1.6×10^{12}
Beam screen + graphite collimators	2.5×10^{10}	3.3×10^{10}
Beam screen + Molybdenum-Graphite collimators	0.9×10^{11}	1.10×10^{11}
Beam screen + Molybdenum-Graphite collimators + interconnects	0.9×10^{11}	1.06×10^{11}

Table 3.9: TMCI threshold estimated with Sacherer formula for the FCChh study cases.

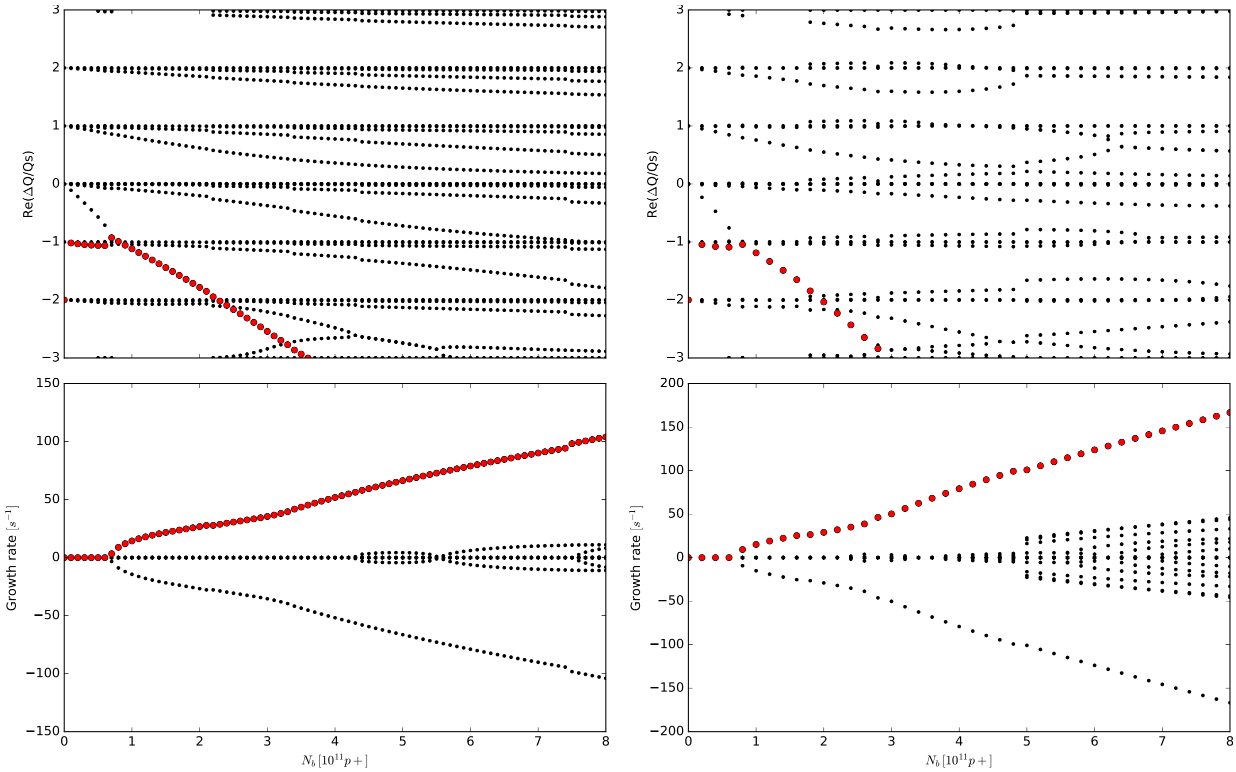

(a) BS + MoGr collimators

(b) BS + MoGr collimators + interconnects

Figure 3.17: Tune shifts and growth rates versus bunch intensity obtained with DELPHI simulations for the cases Beam screen + Molybdenum-Graphite collimators and Beam screen + Molybdenum-Graphite collimators + interconnects. Red points indicate the most unstable mode (eigenvalue with the largest imaginary part).

of mode 0. In figure 3.16a we see that for intensities higher than 8×10^{11} protons per bunch mode -1 starts to shift up. Moreover mode 0 tune shift is not linear on the whole intensity range, and the tune shift slope is steeper for high intensities. This influence of modes 0 and -1 on one another tend to lower the TMCI threshold. These remarks can also explain the discrepancies observed with the cases including collimators.

These first impedance models show the strong impact of the collimation system on the beam stability. With Molybdenum-Graphite collimators, the intensity threshold after which an instability appears is of the same order as the intended single bunch intensity. Having a positive chromaticity and adding dampers in the machine would improve the instability threshold, however the dynamic aperture available for the beam would be reduced and non-linearities would arise. For these reasons we seek to reduce the machine's impedance.

Conclusion

This report gave a first picture of bunched beam instabilities in circular accelerators. These perturbations in the beam structure are caused by electromagnetic fields created by the interaction of the beam with its surroundings. An unstable beam can see its properties deteriorate or even be lost in the machine.

A first part exposed the simplified accelerator model used in this work and the concepts of wakefields and impedances which allow to model the interactions of the beam induced electromagnetic fields with the surrounding environment.

A second part exposed the Vlasov equation formalism used in DELPHI. With this equation, derived from Boltzmann one, and with the perturbation formalism we obtain an eigenvalues system. This system represents how the different instability modes develops themselves and interact for a given impedance model. The eigenvalues and eigenvectors obtained when solving the eigensystem provide informations on the tune shifts, the instability growth rate and the observable signal at a beam position monitor.

A third part showed different studies conducted with DELPHI. Simple impedance models such as the resistive wall or a pure inductive impedance were considered first in order to compare the results with theoretical predictions. The Transverse Mode Coupling Instability which occurs when two different modes couple as the beam intensity increases was studied and its thresholds were estimated for the LHC and the FCC-hh at injection. Finally new longitudinal distributions were implemented in DELPHI allowing to better fit the actual beam profile.

Appendices

Appendix A

Derivation of the eigenvalues problem from Sacherer equation

This part shows the derivation of the eigenvalue problem, starting from the expression of Sacherer integral equation from [14, p. 37]

$$\begin{aligned}(\Omega - Q_{y0}\omega_0 - l\omega_s) R_l(\tau) \ = & -\kappa g_0(\tau) \sum_{l'=-\infty}^{\infty} j^{l'-l} \int_0^{\infty} \mathrm{d}\tau'\tau' R_{l'}(\tau') \ \Bigg(\overbrace{\frac{\mu}{\omega_0} \mathrm{J}_l(-\omega_\xi\tau) \mathrm{J}_{l'}(-\omega_\xi\tau')}^{\text{damper term}} \\ & + \underbrace{\sum_{p=-\infty}^{\infty} Z_y(\omega_p) \mathrm{J}_l((\omega_\xi - \omega_p)\tau) \mathrm{J}_{l'}((\omega_\xi - \omega_p)\tau')}_{\text{impedance term}}\Bigg),\end{aligned} \tag{A.1}$$

and the decomposition over Laguerre polynomials of $R_l(\tau)$ and $g_0(\tau)$

$$R_l(\tau) = \left(\frac{\tau}{\tau_b}\right)^{|l|} \exp\left(-b\tau^2\right) \sum_{n=0}^{\infty} c_{n,l} \mathrm{L}_n^{|l|}\left(a\tau^2\right) \tag{A.2}$$

$$g_0(\tau) = \exp\left(-b\tau^2\right) \sum_{k=0}^{n_0} g_k \mathrm{L}_k^0\left(a\tau^2\right) . \tag{A.3}$$

We decompose the problem into several parts: the right hand side with the damper part and the impedance part and the left hand side. For the right hand side only the damper part will be presented, the derivation steps for the impedance part being identical.

A.1 Right hand side, damper part

This part corresponds to

$$-\kappa g_0(\tau) \sum_{l'=-\infty}^{\infty} j^{l'-l} \int_0^{\infty} \mathrm{d}\tau'\tau' R_{l'}(\tau') \frac{\mu}{\omega_0} \mathrm{J}_l(-\omega_\xi\tau) \mathrm{J}_{l'}(-\omega_\xi\tau') . \tag{A.4}$$

Substituting A.2 and A.3 in A.4 gives

$$-\frac{\kappa\mu}{\omega_0} g_0(\tau) \sum_{l'=-\infty}^{\infty} \sum_{n'=0}^{\infty} j^{l'-l} \tau_b^{-|l'|} c_{n',l'} \mathrm{J}_l(-\omega_\xi\tau) \ \int_0^{\infty} \mathrm{d}\tau'\tau'^{|l'|+1} \exp\left(-b\tau'^2\right) \mathrm{J}_{l'}(-\omega_\xi\tau') \mathrm{L}_{n'}^{|l'|}\left(a\tau'^2\right) . \tag{A.5}$$

Using formula 3 from [7, p. 316]

$$\int_0^{\infty} x^{l'+1}\exp\left(-\eta x^2\right)\mathrm{J}_{l'}(xy)\,\mathrm{L}_{n'}^{|l'|}\left(\alpha\tau'^2\right)\mathrm{d}\tau' = \frac{y^{l'}(\eta-a)^{n'}}{2^{l'+1}\eta^{n'+l'+1}}\exp\left(-\frac{y^2}{4\eta}\right)\mathrm{L}_{n'}^{l'}\left(\frac{\alpha y^2}{4\eta(\alpha-\eta)}\right), \tag{A.6}$$

in the previous equation yields

$$-\frac{\kappa\mu}{\omega_0}g_0(\tau)\sum_{l'=-\infty}^{\infty}\sum_{n'=0}^{\infty} j^{l'-l}c_{n',l'}\mathrm{J}_l(-\omega_\xi\tau)\frac{(b-a)^{n'}(-\omega_\xi)^{|l'|}}{2^{|l'|+1}\tau_b^{|l'|}b^{n'+|l'|+1}}\exp\left(-\frac{\omega_\xi^2}{4b}\right)\mathrm{L}_{n'}^{|l'|}\left(\frac{a\omega_\xi^2}{4b(a-b)}\right), \tag{A.7}$$

and expanding $g_0(\tau)$ gives

$$\begin{aligned}-\frac{\kappa\mu}{\omega_0}\sum_{l'=-\infty}^{\infty}\sum_{n'=0}^{\infty}\sum_{k=0}^{n_0} & j^{l'-l}c_{n',l'}\mathrm{J}_l(-\omega_\xi\tau)\,\mathrm{L}_k^0\left(a\tau^2\right)\exp\left(-b\tau^2\right)\\ & \frac{g_k(b-a)^{n'}(-\omega_\xi)^{|l'|}}{2^{|l'|+1}\tau_b^{|l'|}b^{n'+|l'|+1}}\exp\left(-\frac{\omega_\xi^2}{4b}\right)\mathrm{L}_{n'}^{|l'|}\left(\frac{a\omega_\xi^2}{4b(a-b)}\right).\end{aligned} \tag{A.8}$$

This whole term is then multiplied by the weight function

$$2a^{|l|+1}\tau^{|l|+1}\mathrm{L}_n^{|l|}\left(a\tau^2\right)\exp\left((b-a)\tau^2\right), \tag{A.9}$$

giving us

$$\begin{aligned}-\frac{\kappa\mu}{\omega_0}\sum_{l'=-\infty}^{\infty}\sum_{n'=0}^{\infty}\sum_{k=0}^{n_0} & j^{l'-l}c_{n',l'}\mathrm{J}_l(-\omega_\xi\tau)\,\mathrm{L}_k^0\left(a\tau^2\right)\exp\left(a\tau^2\right)\mathrm{L}_n^{|l|}\left(a\tau^2\right)(a\tau)^{|l|+1}\\ & \frac{g_k(b-a)^{n'}(-\omega_\xi)^{|l'|}}{2^{|l'|}\tau_b^{|l'|}b^{n'+|l'|+1}}\mathrm{L}_{n'}^{|l'|}\left(\frac{a\omega_\xi^2}{4b(a-b)}\right).\end{aligned} \tag{A.10}$$

This expression is then integrated over τ and using formula 8 from [1, p. 43]

$$\begin{aligned}&\int_0^{+\infty} x^{\nu+1/2}\sqrt{xy}\,\mathrm{J}_\nu(xy)\,\mathrm{L}_i^{\nu-\sigma}\left(\alpha x^2\right)\mathrm{L}_j^{\sigma}\left(\alpha x^2\right)\exp\left(-\alpha x^2\right)\mathrm{d}x =\\ &\frac{(-1)^{i+j}\,y^{\nu+1/2}}{(2\alpha)^{\nu+1}}\mathrm{L}_i^{i-j+\nu-\sigma}\left(\frac{y^2}{4\alpha}\right)\mathrm{L}_j^{-i+j+\sigma}\left(\frac{y^2}{4\alpha}\right)\exp\left(-\frac{y^2}{4\alpha}\right),\end{aligned} \tag{A.11}$$

giving finally for the damper term

$$\begin{aligned}-\frac{\kappa\mu}{\omega_0}\sum_{l'=-\infty}^{\infty}\sum_{n'=0}^{\infty}\sum_{k=0}^{n_0} & j^{l'-l+1}c_{n',l'}\frac{(-1)^{n+k+1}\,g_k(b-a)^{n'}(-\omega_\xi)^{|l'|+|l|}}{2^{|l'|+|l|}\tau_b^{|l'|}b^{n'+|l'|+1}}\\ & \mathrm{L}_k^{k-n}\left(\frac{\omega_\xi^2}{4a}\right)\mathrm{L}_n^{n-k+|l|}\left(\frac{\omega_\xi^2}{4a}\right)\mathrm{L}_{n'}^{|l'|}\left(\frac{a\omega_\xi^2}{4b(a-b)}\right).\end{aligned} \tag{A.12}$$

A.2 Left hand side

The operations performed on the right hand side and described in the previous section are reproduced on the left hand side. Starting from

$$(\Omega - Q_{y0}\omega_0 - l\omega_s)\,R_l(\tau), \tag{A.13}$$

expanding $R_l(\tau)$ yields

$$(\Omega - Q_{y0}\omega_0 - l\omega_s)\left(\frac{\tau}{\tau_b}\right)^{|l|}\exp\left(-b\tau^2\right)\sum_{n'=0}^{\infty}c_{n',l}\mathrm{L}_{n'}^{|l|}\left(a\tau^2\right) \tag{A.14}$$

This term has to be multiplied by the weight function

$$2a^{|l|+1}\tau^{|l|+1}\mathrm{L}_n^{|l|}\left(a\tau^2\right)\exp\left(\left(b-a\right)\tau^2\right)\,, \tag{A.15}$$

and integrated over τ. The left hand side is now written

$$\begin{aligned}
&\sum_{n'=0}^{\infty}\left(\Omega-Q_{y0}\omega_0-l\omega_s\right)c_{n',l}\tau_b^{-|l|}\int_0^{\infty}2\tau\left(a\tau^2\right)^{|l|}\exp\left(a\tau^2\right)\mathrm{L}_n^{|l|}\left(a\tau^2\right)\mathrm{L}_{n'}^{|l|}\left(a\tau^2\right)\mathrm{d}\tau\\
=&\sum_{n'=0}^{\infty}\left(\Omega-Q_{y0}\omega_0-l\omega_s\right)c_{n',l}\tau_b^{-|l|}\int_0^{\infty}\left(a\tau^2\right)^{|l|}\exp\left(a\tau^2\right)\mathrm{L}_n^{|l|}\left(a\tau^2\right)\mathrm{L}_{n'}^{|l|}\left(a\tau^2\right)\mathrm{d}\left(a\tau^2\right)\,.
\end{aligned} \tag{A.16}$$

The generalized Laguerre polynomials are orthogonal on the interval $[0;+\infty[$ for the weight function $\exp\left(-x\right)x^l$:

$$\int_0^{\infty}\exp\left(-x\right)x^l\mathrm{L}_n^l\left(x\right)\mathrm{L}_{n'}^l\left(x\right)=\frac{(n+l)!}{n!}\delta_{n,n'}\,. \tag{A.17}$$

Finally the left hand side of equation A.1 can be written

$$\sum_{n'=0}^{\infty}\left(\Omega-Q_{y0}\omega_0-l\omega_s\right)c_{n',l}\frac{(n'+|l|)!}{\tau_b^{|l|}n'!}\delta_{n,n'}\,, \tag{A.18}$$

and when selecting a value for n:

$$\left(\Omega-Q_{y0}\omega_0-l\omega_s\right)c_{n,l}\frac{(n'+|l|)!}{\tau_b^{|l|}n!} \tag{A.19}$$

Bibliography

[1] Harry Bateman. *Tables of Integral Transforms.* Vol. II. McGraw-Hill Book Company, New-York, 1954.

[2] Alessandro Bertarelli et al. "Novel Materials for Collimators at LHC and its Upgrades". In: *54th ICFA Advanced Beam Dynamics Workshop on High-Intensity, High Brightness and High Power Hadron Beams.* Nov. 2014.

[3] Nicolò Biancacci. "Improved techniques of impedance calculation and localization in particle accelerators". PhD thesis. Universita degli Studi di Roma "La Sapienza", 2014.

[4] Frederick Bordry. "LHC and Future High-Energy Circular Colliders". Seminar at the Joint Universities Accelerator School. 2016. URL: https://indico.cern.ch/event/471931/contribution/252.

[5] Oliver Sim Brüning et al. *LHC Design Report.* Vol. 1. CERN, 2004.

[6] Xavier Buffat. "Impedance driven instabilities in the early stage of the FCC-hh design studies". Presentation at FCC-hh impedance meeting. June 2016. URL: https://indico.cern.ch/event/540975/contributions/2201370/attachments/1288978/1918728/CollectiveEffect-FCChh.pdf.

[7] Alexander Wu Chao. *Physics of collective beam instabilities in high energy accelerators.* New York, NY: Wiley, 1993.

[8] Diego Ferrazza. "FCC-hh interconnects model". Private communication. July 2016.

[9] Jean-Louis Laclare. "Bunched beam coherent instabilities". In: *CAS - CERN Accelerator School: Accelerator Physics.* 1987.

[10] Andrea Latina. "Introduction to Transverse Beam Dynamics". Course at the Joint Universities Accelerator School. Jan. 2016. URL: https://indico.cern.ch/event/471931/contributions/1149878/attachments/1214721/1794333/Lectures.pdf.

[11] Elias Métral. "Bunched-beam transverse coherent instabilities". Course at the USPAS. June 2009. URL: http://emetral.web.cern.ch.

[12] Elias Métral. "Shifts of the head-tail modes due to a constant inductive impedance". Presentation at HSC meeting. Aug. 2016. URL: https://espace.cern.ch/be-dep/ABP/HSC/Meetings/HeadTailModesShifts_ConstantInductiveImpedance_EM_08-08-2016.pdf.

[13] Mauro Migliorati. "Wake Fields and Instabilities". Course at the Joint Universities Accelerator School. Jan. 2016. URL: https://indico.cern.ch/event/471931/contribution/84.

[14] Nicolas Mounet. "DELPHI: an analytic Vlasov solver for impedance-drive modes". Presentation at HSC meeting. Apr. 2014. URL: https://espace.cern.ch/be-dep/ABP/HSC/Meetings/DELPHI-expanded.pdf.

[15] King-Yuen Ng. *Physics of Intensity Dependent Beam Instabilities.* Fermilab, 2005.

[16] Frank Sacherer. "Transverse bunched beam instabilities - Theory". In: *9th International Conference on High-energy Accelerators.* 1974.

[17] Daniel Schulte. "FCC-hh impedance introductory presentation". Presentation at FCC-hh impedance meeting. June 2016. URL: https://indico.cern.ch/event/540975/contributions/2201368/attachments/1288937/1918650/Impedance.pdf.

Résumé

Les faisceaux de fortes intensités circulant dans les accélérateurs peuvent être perturbés par les champs électromagnétiques créés par le faisceau lui-même lors de l'interaction avec son environnement.Ces perturbations peuvent potentiellement rendre le faisceau instable et conduire à des pertes de particules.

Les concepts de champ électromagnétique de sillage et d'impédance permettent d'étudier l'interaction du faisceau avec son environnement et sont le point de départ des études numériques de stabilité du faisceau. Une moyen d'évaluer celle-ci avec un modèle d'impédance est de résoudre l'équation de Vlasov à l'aide d'une approche perturbative. Les modes d'instabilités se développant au sein du faisceau sont associés aux solutions d'un problème aux valeurs propres.

Ce travail présentera le formalisme utilisé par le code DELPHI (Discrete Expansion over Laguerre Polynomials and Headtail modes) qui permet d'extraire les modes propres instables et les vecteur propres correspondant, directement comparable avec les signaux des BPM (Beam Position Monitors) installés sur la machine. Nous présenterons les études menées avec DELPHI évaluant l'impact de différentes distributions longitudinales sur le changement de tune et sur l'instabilité de couplage de modes transversaux pour le LHC et FCC-hh. Des études de base avec des modèles classiques d'impédance (large bande, mur résistif) seront aussi présentées.

Keywords : Accélérateur, Instabilités faisceau, Équation de Vlasov

Abstract

High intensity particle beams circulating in accelerators can be perturbed by the electromagnetic field created by the beam itself and the interaction with the surrounding environment. This perturbation can potentially drive the whole beam unstable and conduct to particle losses.

The concepts of wakefield and impedance allow to study the electromagnetic interaction of the beam with its surroundings and are the starting point to perform numerical beam stability simulations. A way to study beam stability using an impedance model is to solve the Vlasov equation with a perturbative approach: the unstable modes developing in a beam are associated to the solution of an eigenvalue problem.

In this work we will present the formalism used in the simulation code DELPHI (Discrete Expansion over Laguerre Polynomials and Headtail modes) that allows to extract the most unstable eigenmodes and the corresponding eigenvectors, directly comparable with the signal measurable with beam position monitors in the machine. We will present studies performed with DELPHI on the effect of different particle distributions on the tune of the machine, and on the Transverse Mode Coupling Instability (TMCI) threshold for the LHC and FCC-hh. Basic studies with classical impedance models (e.g. resistive wall, broad band impedance) will be presented as well.

Keywords : Accelerator, Beam instability, Vlasov equation